All-sky search for periodic gravitational waves in LIGO S4 data

B. Abbott,[15] R. Abbott,[15] R. Adhikari,[15] J. Agresti,[15] P. Ajith,[2] B. Allen,[2,50] R. Amin,[19] S. B. Anderson,[15]
W. G. Anderson,[50] M. Arain,[39] M. Araya,[15] H. Armandula,[15] M. Ashley,[4] S. Aston,[38] P. Aufmuth,[14] C. Aulbert,[1] S. Babak,[1]
S. Ballmer,[15] H. Bantilan,[8] B. C. Barish,[15] C. Barker,[16] D. Barker,[16] B. Barr,[40] P. Barriga,[49] M. A. Barton,[40] K. Bayer,[18]
K. Belczynski,[25] J. Betzwieser,[18] P. T. Beyersdorf,[28] B. Bhawal,[15] I. A. Bilenko,[22] G. Billingsley,[15] R. Biswas,[50]
E. Black,[15] K. Blackburn,[15] L. Blackburn,[18] D. Blair,[49] B. Bland,[16] J. Bogenstahl,[40] L. Bogue,[17] R. Bork,[15] V. Boschi,[15]
S. Bose,[51] P. R. Brady,[50] V. B. Braginsky,[22] J. E. Brau,[43] M. Brinkmann,[2] A. Brooks,[37] D. A. Brown,[15,6] A. Bullington,[31]
A. Bunkowski,[2] A. Buonanno,[41] O. Burmeister,[2] D. Busby,[15] R. L. Byer,[31] L. Cadonati,[18] G. Cagnoli,[40] J. B. Camp,[23]
J. Cannizzo,[23] K. Cannon,[50] C. A. Cantley,[40] J. Cao,[18] L. Cardenas,[15] M. M. Casey,[40] G. Castaldi,[46] C. Cepeda,[15]
E. Chalkley,[40] P. Charlton,[9] S. Chatterji,[15] S. Chelkowski,[2] Y. Chen,[1] F. Chiadini,[45] D. Chin,[42] E. Chin,[49] J. Chow,[4]
N. Christensen,[8] J. Clark,[40] P. Cochrane,[2] T. Cokelaer,[7] C. N. Colacino,[38] R. Coldwell,[39] R. Conte,[45] D. Cook,[16]
T. Corbitt,[18] D. Coward,[49] D. Coyne,[15] J. D. E. Creighton,[50] T. D. Creighton,[15] R. P. Croce,[46] D. R. M. Crooks,[40]
A. M. Cruise,[38] A. Cumming,[40] J. Dalrymple,[32] E. D'Ambrosio,[15] K. Danzmann,[14,2] G. Davies,[7] D. DeBra,[31]
J. Degallaix,[49] M. Degree,[31] T. Demma,[46] V. Dergachev,[42] S. Desai,[33] R. DeSalvo,[15] S. Dhurandhar,[13] M. Díaz,[34]
J. Dickson,[4] A. Di Credico,[32] G. Diederichs,[14] A. Dietz,[7] E. E. Doomes,[30] R. W. P. Drever,[5] J.-C. Dumas,[49] R. J. Dupuis,[15]
J. G. Dwyer,[10] P. Ehrens,[15] E. Espinoza,[15] T. Etzel,[15] M. Evans,[15] T. Evans,[17] S. Fairhurst,[7,15] Y. Fan,[49] D. Fazi,[15]
M. M. Fejer,[31] L. S. Finn,[33] V. Fiumara,[45] N. Fotopoulos,[50] A. Franzen,[14] K. Y. Franzen,[39] A. Freise,[38] R. Frey,[43]
T. Fricke,[44] P. Fritschel,[18] V. V. Frolov,[17] M. Fyffe,[17] V. Galdi,[46] J. Garofoli,[16] I. Gholami,[1] J. A. Giaime,[17,19]
S. Giampanis,[44] K. D. Giardina,[17] K. Goda,[18] E. Goetz,[42] L. M. Goggin,[15] G. González,[19] S. Gossler,[4] A. Grant,[40]
S. Gras,[49] C. Gray,[16] M. Gray,[4] J. Greenhalgh,[27] A. M. Gretarsson,[11] R. Grosso,[34] H. Grote,[2] S. Grunewald,[1]
M. Guenther,[16] R. Gustafson,[42] B. Hage,[14] D. Hammer,[50] C. Hanna,[19] J. Hanson,[17] J. Harms,[2] G. Harry,[18] E. Harstad,[43]
T. Hayler,[27] J. Heefner,[15] I. S. Heng,[40] A. Heptonstall,[40] M. Heurs,[2] M. Hewitson,[2] S. Hild,[14] E. Hirose,[32] D. Hoak,[17]
D. Hosken,[37] J. Hough,[40] E. Howell,[49] D. Hoyland,[38] S. H. Huttner,[40] D. Ingram,[16] E. Innerhofer,[18] M. Ito,[43] Y. Itoh,[50]
A. Ivanov,[15] D. Jackrel,[31] B. Johnson,[16] W. W. Johnson,[19] D. I. Jones,[47] G. Jones,[7] R. Jones,[40] L. Ju,[49] P. Kalmus,[10]
V. Kalogera,[25] D. Kasprzyk,[38] E. Katsavounidis,[18] K. Kawabe,[16] S. Kawamura,[24] F. Kawazoe,[24] W. Kells,[15]
D. G. Keppel,[15] F. Ya. Khalili,[22] C. Kim,[25] P. King,[15] J. S. Kissel,[19] S. Klimenko,[39] K. Kokeyama,[24] V. Kondrashov,[15]
R. K. Kopparapu,[19] D. Kozak,[15] B. Krishnan,[1] P. Kwee,[14] P. K. Lam,[4] M. Landry,[16] B. Lantz,[31] A. Lazzarini,[15] B. Lee,[49]
M. Lei,[15] J. Leiner,[51] V. Leonhardt,[24] I. Leonor,[43] K. Libbrecht,[15] P. Lindquist,[15] N. A. Lockerbie,[48] M. Longo,[45]
M. Lormand,[17] M. Lubinski,[16] H. Lück,[14,2] B. Machenschalk,[1] M. MacInnis,[18] M. Mageswaran,[15] K. Mailand,[15]
M. Malec,[14] V. Mandic,[15] S. Marano,[45] S. Márka,[10] J. Markowitz,[18] E. Maros,[15] I. Martin,[40] J. N. Marx,[15] K. Mason,[18]
L. Matone,[10] V. Matta,[45] N. Mavalvala,[18] R. McCarthy,[16] D. E. McClelland,[4] S. C. McGuire,[30] M. McHugh,[21]
K. McKenzie,[4] J. W. C. McNabb,[33] S. McWilliams,[23] T. Meier,[14] A. Melissinos,[44] G. Mendell,[16] R. A. Mercer,[39]
S. Meshkov,[15] C. J. Messenger,[40] D. Meyers,[15] E. Mikhailov,[18] S. Mitra,[13] V. P. Mitrofanov,[22] G. Mitselmakher,[39]
R. Mittleman,[18] O. Miyakawa,[15] S. Mohanty,[34] G. Moreno,[16] K. Mossavi,[2] C. MowLowry,[4] A. Moylan,[4] D. Mudge,[37]
G. Mueller,[39] S. Mukherjee,[34] H. Müller-Ebhardt,[2] J. Munch,[37] P. Murray,[40] E. Myers,[16] J. Myers,[16] T. Nash,[15]
G. Newton,[40] A. Nishizawa,[24] K. Numata,[23] B. O'Reilly,[17] R. O'Shaughnessy,[25] D. J. Ottaway,[18] H. Overmier,[17]
B. J. Owen,[33] Y. Pan,[41] M. A. Papa,[1,50] V. Parameshwaraiah,[16] P. Patel,[15] M. Pedraza,[15] S. Penn,[12] V. Pierro,[46] I. M. Pinto,[46]
M. Pitkin,[40] H. Pletsch,[2] M. V. Plissi,[40] F. Postiglione,[45] R. Prix,[1] V. Quetschke,[39] F. Raab,[16] D. Rabeling,[4] H. Radkins,[16]
R. Rahkola,[43] N. Rainer,[2] M. Rakhmanov,[33] M. Ramsunder,[33] K. Rawlins,[18] S. Ray-Majumder,[50] V. Re,[38] H. Rehbein,[2]
S. Reid,[40] D. H. Reitze,[39] L. Ribichini,[2] R. Riesen,[17] K. Riles,[42] B. Rivera,[16] N. A. Robertson,[15,40] C. Robinson,[7]
E. L. Robinson,[38] S. Roddy,[17] A. Rodriguez,[19] A. M. Rogan,[51] J. Rollins,[10] J. D. Romano,[7] J. Romie,[17] R. Route,[31]
S. Rowan,[40] A. Rüdiger,[2] L. Ruet,[18] P. Russell,[15] K. Ryan,[16] S. Sakata,[24] M. Samidi,[15] L. Sancho de la Jordana,[36]
V. Sandberg,[16] V. Sannibale,[15] S. Saraf,[26] P. Sarin,[18] B. S. Sathyaprakash,[7] S. Sato,[24] P. R. Saulson,[32] R. Savage,[16]
P. Savov,[6] S. Schediwy,[49] R. Schilling,[2] R. Schnabel,[2] R. Schofield,[43] B. F. Schutz,[1,7] P. Schwinberg,[16] S. M. Scott,[4]
A. C. Searle,[4] B. Sears,[15] F. Seifert,[2] D. Sellers,[17] A. S. Sengupta,[7] P. Shawhan,[41] D. H. Shoemaker,[18] A. Sibley,[17]
X. Siemens,[15,6] D. Sigg,[16] S. Sinha,[31] A. M. Sintes,[36,1] B. J. J. Slagmolen,[4] J. Slutsky,[19] J. R. Smith,[2] M. R. Smith,[15]
K. Somiya,[2,1] K. A. Strain,[40] D. M. Strom,[43] A. Stuver,[33] T. Z. Summerscales,[3] K.-X. Sun,[31] M. Sung,[19] P. J. Sutton,[15]
H. Takahashi,[1] D. B. Tanner,[39] M. Tarallo,[15] R. Taylor,[15] R. Taylor,[40] J. Thacker,[17] K. A. Thorne,[33] K. S. Thorne,[6]
A. Thüring,[14] K. V. Tokmakov,[40] C. Torres,[34] C. Torrie,[40] G. Traylor,[17] M. Trias,[36] W. Tyler,[15] D. Ugolini,[35] C. Ungarelli,[38]
K. Urbanek,[31] H. Vahlbruch,[14] M. Vallisneri,[6] C. Van Den Broeck,[7] M. Varvella,[15] S. Vass,[15] A. Vecchio,[38] J. Veitch,[40]

P. Veitch,[37] A. Villar,[15] C. Vorvick,[16] S. P. Vyachanin,[22] S. J. Waldman,[15] L. Wallace,[15] H. Ward,[40] R. Ward,[15] K. Watts,[17] D. Webber,[15] A. Weidner,[2] M. Weinert,[2] A. Weinstein,[15] R. Weiss,[18] S. Wen,[19] K. Wette,[4] J. T. Whelan,[1] D. M. Whitbeck,[33] S. E. Whitcomb,[15] B. F. Whiting,[39] C. Wilkinson,[16] P. A. Willems,[15] L. Williams,[39] B. Willke,[14,2] I. Wilmut,[27] W. Winkler,[2] C. C. Wipf,[18] S. Wise,[39] A. G. Wiseman,[50] G. Woan,[40] D. Woods,[50] R. Wooley,[17] J. Worden,[16] W. Wu,[39] I. Yakushin,[17] H. Yamamoto,[15] Z. Yan,[49] S. Yoshida,[29] N. Yunes,[33] M. Zanolin,[18] J. Zhang,[42] L. Zhang,[15] C. Zhao,[49] N. Zotov,[20] M. Zucker,[18] H. zur Mühlen,[14] and J. Zweizig[15]

(LIGO Scientific Collaboration)

[1]*Albert-Einstein-Institut, Max-Planck-Institut für Gravitationsphysik, D-14476 Golm, Germany*
[2]*Albert-Einstein-Institut, Max-Planck-Institut für Gravitationsphysik, D-30167 Hannover, Germany*
[3]*Andrews University, Berrien Springs, Michigan 49104 USA*
[4]*Australian National University, Canberra, 0200, Australia*
[5]*California Institute of Technology, Pasadena, California 91125, USA*
[6]*Caltech-CaRT, Pasadena, California 91125, USA*
[7]*Cardiff University, Cardiff, CF24 3AA, United Kingdom*
[8]*Carleton College, Northfield, Minnesota 55057, USA*
[9]*Charles Sturt University, Wagga Wagga, NSW 2678, Australia*
[10]*Columbia University, New York, New York 10027, USA*
[11]*Embry-Riddle Aeronautical University, Prescott, Arizona 86301 USA*
[12]*Hobart and William Smith Colleges, Geneva, New York 14456, USA*
[13]*Inter-University Centre for Astronomy and Astrophysics, Pune - 411007, India*
[14]*Leibnitz Universität Hannover, D-30167 Hannover, Germany*
[15]*LIGO - California Institute of Technology, Pasadena, California 91125, USA*
[16]*LIGO Hanford Observatory, Richland, Washington 99352, USA*
[17]*LIGO Livingston Observatory, Livingston, Louisiana 70754, USA*
[18]*LIGO - Massachusetts Institute of Technology, Cambridge, Massachusetts 02139, USA*
[19]*Louisiana State University, Baton Rouge, Louisiana 70803, USA*
[20]*Louisiana Tech University, Ruston, Louisiana 71272, USA*
[21]*Loyola University, New Orleans, Louisiana 70118, USA*
[22]*Moscow State University, Moscow, 119992, Russia*
[23]*NASA/Goddard Space Flight Center, Greenbelt, Maryland 20771, USA*
[24]*National Astronomical Observatory of Japan, Tokyo 181-8588, Japan*
[25]*Northwestern University, Evanston, Illinois 60208, USA*
[26]*Rochester Institute of Technology, Rochester, New York 14623, USA*
[27]*Rutherford Appleton Laboratory, Chilton, Didcot, Oxon OX11 0QX United Kingdom*
[28]*San Jose State University, San Jose, California 95192, USA*
[29]*Southeastern Louisiana University, Hammond, Louisiana 70402, USA*
[30]*Southern University and A&M College, Baton Rouge, Louisiana 70813, USA*
[31]*Stanford University, Stanford, California 94305, USA*
[32]*Syracuse University, Syracuse, New York 13244, USA*
[33]*The Pennsylvania State University, University Park, Pennsylvania 16802, USA*
[34]*The University of Texas at Brownsville and Texas Southmost College, Brownsville, Texas 78520, USA*
[35]*Trinity University, San Antonio, Texas 78212, USA*
[36]*Universitat de les Illes Balears, E-07122 Palma de Mallorca, Spain*
[37]*University of Adelaide, Adelaide, SA 5005, Australia*
[38]*University of Birmingham, Birmingham, B15 2TT, United Kingdom*
[39]*University of Florida, Gainesville, Florida 32611, USA*
[40]*University of Glasgow, Glasgow, G12 8QQ, United Kingdom*
[41]*University of Maryland, College Park, Maryland 20742 USA*
[42]*University of Michigan, Ann Arbor, Michigan 48109, USA*
[43]*University of Oregon, Eugene, Oregon 97403, USA*
[44]*University of Rochester, Rochester, New York 14627, USA*
[45]*University of Salerno, 84084 Fisciano (Salerno), Italy*
[46]*University of Sannio at Benevento, I-82100 Benevento, Italy*
[47]*University of Southampton, Southampton, SO17 1BJ, United Kingdom*
[48]*University of Strathclyde, Glasgow, G1 1XQ, United Kingdom*
[49]*University of Western Australia, Crawley, Washington 6009, Australia, USA*
[50]*University of Wisconsin-Milwaukee, Milwaukee, Wisconsin 53201, USA*

[51]*Washington State University, Pullman, Washington 99164, USA*

We report on an all-sky search with the LIGO detectors for periodic gravitational waves in the frequency range 50–1000 Hz and with the frequency's time derivative in the range -1×10^{-8} Hz s^{-1} to zero. Data from the fourth LIGO science run (S4) have been used in this search. Three different semicoherent methods of transforming and summing strain power from short Fourier transforms (SFTs) of the calibrated data have been used. The first, known as StackSlide, averages normalized power from each SFT. A ''weighted Hough'' scheme is also developed and used, which also allows for a multi-interferometer search. The third method, known as PowerFlux, is a variant of the StackSlide method in which the power is weighted before summing. In both the weighted Hough and PowerFlux methods, the weights are chosen according to the noise and detector antenna-pattern to maximize the signal-to-noise ratio. The respective advantages and disadvantages of these methods are discussed. Observing no evidence of periodic gravitational radiation, we report upper limits; we interpret these as limits on this radiation from isolated rotating neutron stars. The best population-based upper limit with 95% confidence on the gravitational-wave strain amplitude, found for simulated sources distributed isotropically across the sky and with isotropically distributed spin axes, is 4.28×10^{-24} (near 140 Hz). Strict upper limits are also obtained for small patches on the sky for best-case and worst-case inclinations of the spin axes.

I. INTRODUCTION

We report on a search with the LIGO (Laser Interferometer Gravitational-wave Observatory) detectors [1,2] for periodic gravitational waves in the frequency range 50–1000 Hz and with the frequency's time derivative in the range -1×10^{-8} Hz s^{-1} to zero. The search is carried out over the entire sky using data from the fourth LIGO science run (S4). Isolated rotating neutron stars in our galaxy are the prime target.

Using data from earlier science runs, the LIGO Scientific Collaboration (LSC) has previously reported on searches for periodic gravitational radiation, using a long-period coherent method to target known pulsars [3–5], using a short-period coherent method to target Scorpius X-1 in selected bands and search the entire sky in the 160.0–728.8 Hz band [6], and using a long-period semi-coherent method to search the entire sky in the 200–400 Hz band [7]. Einstein@Home, a distributed home computing effort running under the BOINC architecture [8], has also been searching the entire sky using a coherent first stage, followed by a simple coincidence stage [9]. In comparison, this paper: (1) examines more sensitive data; (2) searches over a larger range in frequency and its derivative; and (3) uses three alternative semicoherent methods for summing measured strain powers to detect excess power from a continuous gravitational-wave signal.

The first purpose of this paper is to present results from our search for periodic gravitational waves in the S4 data. Over the LIGO frequency band of sensitivity, the S4 all-sky upper limits presented here are approximately an order of magnitude better than published previously from earlier science runs [6,7]. After following up on outliers in the data, we find that no candidates survive, and thus report upper limits. These are interpreted as limits on radiation from rotating neutron stars, which can be expressed as

functions of the star's ellipticity and distance, allowing for an astrophysical interpretation. The best population-based upper limit with 95% confidence on the gravitational-wave strain amplitude, found for simulated sources distributed isotropically across the sky and with isotropically distributed spin axes, is 4.28×10^{-24} (near 140 Hz). Strict upper limits are also obtained for small patches on the sky for best-case and worst-case inclinations of the spin axes.

The second purpose of this paper, along with the previous coherent [6] and semicoherent [7] papers, is to lay the foundation for the methods that will be used in future searches. It is well known that the search for periodic gravitational waves is computationally bound; to obtain optimal results will require a hierarchical approach that uses coherent and semicoherent stages [10–13]. A fifth science run (S5), which started in November 2005, is generating data at initial LIGO's design sensitivity. We plan to search this data using the best methods possible, based on what is learned from this and previous analyses.

In the three methods considered here, one searches for cumulative excess power from a hypothetical periodic gravitational-wave signal by examining successive spectral estimates based on short Fourier transforms (SFTs) of the calibrated detector strain data channel, taking into account the Doppler modulations of detected frequency due to the Earth's rotational and orbital motion with respect to the solar system barycenter (SSB), and the time derivative of the frequency intrinsic to the source. The simplest method presented, known as ''StackSlide'' [12–15], averages normalized power from each SFT. In the Hough method reported previously [7,10], referred to here as ''standard Hough,'' the sum is of binary zeroes or ones, where a SFT contributes unity if the power exceeds a normalized power threshold. In this paper a ''weighted Hough'' scheme,

henceforth also referred to as "Hough," has been developed and is similar to that described in Ref. [16]. This scheme also allows for a multi-interferometer search. The third method, known as "PowerFlux" [17], is a variant of the StackSlide method in which the power is weighted before summing. In both the weighted Hough and PowerFlux methods, the weights are chosen according to the noise and detector antenna pattern to maximize the signal-to-noise ratio.

The Hough method is computationally faster and more robust against large transient power artifacts, but is slightly less sensitive than StackSlide for stationary data [7,15]. The PowerFlux method is found in most frequency ranges to have better detection efficiency than the StackSlide and Hough methods, the exceptions occurring in bands with large nonstationary artifacts, for which the Hough method proves more robust. However, the StackSlide and Hough methods can be made more sensitive by starting with the maximum likelihood statistic (known as the $\mathcal{F}$-statistic [6,10,18]) rather than SFT power as the input data, though this improvement comes with increased computational cost. The trade-offs among the methods mean that each could play a role in our future searches.

In brief, this paper makes several important contributions. It sets the best all-sky upper limits on periodic gravitational waves to date, and shows that these limits are becoming astrophysically interesting. It also introduces methods that are crucial to the development of our future searches.

This paper is organized as follows: Sec. II briefly describes the LIGO interferometers, focusing on improvements made for the S4 data run, and discusses the sensitivity and relevant detector artifacts. Section III precisely defines the waveforms we seek and the associated assumptions we have made. Section IV gives a detailed description of the three analysis methods used and summarizes their similarities and differences, while Sec. V gives the details of their implementations and the pipelines used. Section VI discusses the validation of the software and, as an end-to-end test, shows the detection of simulated pulsar signals injected into the data stream at the hardware level. Section VII describes the search results, and Sec. VIII compares the results from the three respective methods. Section IX concludes with a summary of the results, their astrophysical implications, and future plans.

II. THE LIGO DETECTOR NETWORK AND THE S4 SCIENCE RUN

The LIGO detector network consists of a 4-km interferometer in Livingston, Louisiana (called L1) and two interferometers in Hanford, Washington, one 4-km and another 2-km (H1 and H2, respectively).

The data analyzed in this paper were produced during LIGO's 29.5-day fourth science run (S4) [19]. This run started at noon Central Standard Time (CST) on February 22 and ended at midnight CST on March 23, 2005. During the run, all three LIGO detectors had displacement spectral amplitudes near 2.5×10^{-19} m Hz$^{-1/2}$ in their most sensitive frequency band near 150 Hz. In units of gravitational-wave strain amplitude, the sensitivity of H2 is roughly a factor of 2 worse than that of H1 and L1 over much of the search band. The typical strain sensitivities in this run were within a factor of 2 of the design goals. Figure 1 shows representative strain spectral noise densities for the three interferometers during the run. As discussed in Sec. V below, however, nonstationarity of the noise was significant.

Changes to the interferometers before the S4 run included the following improvements [19]:

(i) Installation of active seismic isolation of support structures at Livingston to cope with high anthropogenic ground motion in the 1–3 Hz band.

(ii) Thermal compensation with a CO_2 laser of mirrors subject to thermal lensing from the primary laser beam to a greater or lesser degree than expected.

(iii) Replacement of a synthesized radio frequency oscillator for phase modulation with a crystal oscillator before S4 began (H1) and midway through the S4 run (L1), reducing noise substantially above 1000 Hz, and eliminating a comb of ∼37 Hz lines. (The crystal oscillator replacement for H2 occurred after the S4 run.)

(iv) Lower-noise mirror-actuation electronics (H1, H2, and L1).

(v) Higher-bandwidth laser frequency stabilization (H1, H2, and L1) and intensity stabilization (H1 and L1).

(vi) Installation of radiation pressure actuation of mirrors for calibration validation (H1).

(vii) Commissioning of complete alignment control system for the L1 interferometer (already implemented for H1 and H2 in S3 run).
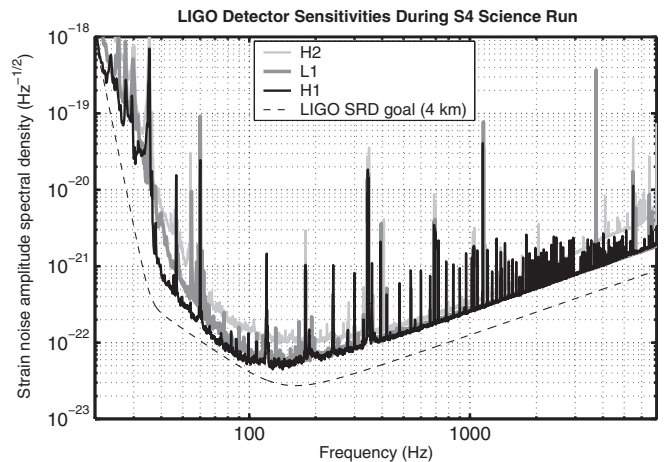

FIG. 1. Median amplitude strain noise spectral densities from the three LIGO interferometers during the S4 run, along with the initial LIGO design sensitivity goal.

(viii) Refurbishment of lasers and installation of photo-diodes and electronics to permit interferometer operation with increased laser power (H1, H2, and L1).

(ix) Mitigation of electromagnetic interference (H1, H2, and L1) and acoustic interference (L1).

The data were acquired and digitized at a rate of 16 384 Hz. Data acquisition was periodically interrupted by disturbances such as seismic transients, reducing the net running time of the interferometers. The resulting duty factors for the interferometers were 81% for H1 and H2, and 74% for L1. While the H1 and H2 duty factors were somewhat higher than those in previous science runs, the L1 duty factor was dramatically higher than the $\simeq 40\%$ typical of the past, thanks to the increased stability from the installation of the active seismic isolation system at Livingston.

III. SIGNAL WAVEFORMS

The general form of a gravitational-wave signal is described in terms of two orthogonal transverse polarizations defined as "+" with waveform $h_+(t)$ and "×" with waveform $h_\times(t)$. The calibrated response seen by an interferometric gravitational-wave detector is then [18]

$$h(t) = F_+(t, \alpha, \delta, \psi)h_+(t) + F_\times(t, \alpha, \delta, \psi)h_\times(t), \quad (1)$$

where t is time in the detector frame, α is the source right ascension, δ is the source declination, ψ is the polarization angle of the wave, and $F_{+,\times}$ are the detector antenna pattern functions for the two orthogonal polarizations. For periodic (nearly pure sinusoidal) gravitational waves, which in general are elliptically polarized, the individual components $h_{+,\times}$ have the form

$$h_+(t) = A_+ \cos\Phi(t), \quad (2)$$

$$h_\times(t) = A_\times \sin\Phi(t), \quad (3)$$

where A_+ and $A_\times$ are the amplitudes of the two polarizations, and $\Phi(t)$ is the phase of the signal at the detector. (One can also define the initial phase of the signal, Φ_0, but in this paper it can be taken to be an unknown and irrelevant constant).

For an isolated quadrupolar gravitational-wave emitter, characterized by a rotating triaxial-ellipsoid mass distribution, the amplitudes A_+ and $A_\times$ are related to the inclination angle of the source, ι, and the wave amplitude, h_0, by

$$A_+ = \tfrac{1}{2}h_0(1 + \cos^2\iota), \quad (4)$$

$$A_\times = h_0\cos\iota, \quad (5)$$

where ι is the angle of its spin axis with respect to the line of sight between source and detector. For such a star, the gravitational-wave frequency, f, is twice the rotation frequency, ν, and the amplitude h_0 is given by

$$h_0 = \frac{16\pi^2 G}{c^4} \frac{I\epsilon\nu^2}{d}. \quad (6)$$

Here d is the distance to the star, I is the principal moment of inertia with respect to its spin axis, and ϵ is the equatorial ellipticity of the star [18]. Assuming that all of the frequency's derivative, $\dot{f}$, is due to emission of gravitational radiation and that I takes the canonical value 10^{38} kg m^2, we can relate ϵ to f and $\dot{f}$ and use Eq. (6) to obtain

$$h_{sd} = 4.54 \times 10^{-24}\left(\frac{1 \text{ kpc}}{d}\right)\left(\frac{250 \text{ yr}}{-f/(4\dot{f})}\right)^{1/2}, \quad (7)$$

by eliminating ϵ, or

$$\epsilon_{sd} = 7.63 \times 10^{-5}\left(\frac{-\dot{f}}{10^{-10} \text{ Hz s}^{-1}}\right)^{1/2}\left(\frac{100 \text{ Hz}}{f}\right)^{5/2}, \quad (8)$$

by eliminating d. These are referred to, respectively, as the *spin-down limits* on strain and ellipticity. (See Eqs. (8), (9), and (19) of [6] for more details of the derivation.)

Note that the methods used in this paper are sensitive to periodic signals from any type of isolated gravitational-wave source (e.g., freely precessing or oscillating neutron stars as well as triaxial ones), though we present upper limits in terms of h_0 and ϵ. Because we use semicoherent methods, only the instantaneous signal frequency in the detector reference frame, $2\pi f(t) = d\Phi(t)/dt$, needs to be calculated. In the detector reference frame this can, to a very good approximation, be related to the instantaneous SSB-frame frequency $\hat{f}(t)$ by [7]

$$f(t) - \hat{f}(t) = \hat{f}(t)\frac{\mathbf{v}(t)\cdot\hat{\mathbf{n}}}{c}, \quad (9)$$

where $\mathbf{v}(t)$ is the detector's velocity with respect to the SSB frame, and $\hat{\mathbf{n}}$ is the unit-vector corresponding to the sky location of the source. In this analysis, we search for $\hat{f}(t)$ signals well described by a nominal frequency $\hat{f}_0$ at the start of the S4 run t_0 and a constant first time derivative $\dot{f}$, such that

$$\hat{f}(t) = \hat{f}_0 + \dot{f}(t - t_0). \quad (10)$$

These equations ignore corrections to the time interval $t - t_0$ at the detector compared with that at the SSB and relativistic corrections. These corrections are negligible for the one month semicoherent searches described here, though the LSC Algorithm Library (LAL) code [20] used by our searches does provide routines that make all the corrections needed to provide a timing accuracy of 3 μs. (The LAL code also can calculate $f(t)$ for signals arriving from periodic sources in binary systems. Including unknown orbital parameters in the search, however, would greatly increase the computational cost or require new methods beyond the scope of this article.)

IV. OVERVIEW OF THE METHODS

A. Similarities and differences

The three different analysis methods presented here have many features in common, but also have important differences, both major and minor. In this section we give a brief overview of the methods.

1. The parameter space

All three methods are based on summing measures of strain power from many SFTs that have been created from 30-minute intervals of calibrated strain data. Each method also corrects explicitly for sky-position dependent Doppler modulations of the apparent source frequency due to the Earth's rotation and its orbital motion around the SSB, and the frequency's time derivative, intrinsic to the source (see Fig. 2). This requires a search in a four-dimensional parameter space; a template in the space refers to a set of values: $\lambda = \{\hat{f}_0, \dot{f}, \alpha, \delta\}$. The third method, PowerFlux, also searches explicitly over polarization angle, so that $\lambda = \{\hat{f}_0, \dot{f}, \alpha, \delta, \psi\}$.

All three methods search for initial frequency $\hat{f}_0$ in the range 50–1000 Hz with a uniform grid spacing equal to the size of a SFT frequency bin,

$$\delta f = \frac{1}{T_{\text{coh}}} = 5.556 \times 10^{-4} \text{ Hz}, \qquad (11)$$

where T_{coh} is the time-baseline of each SFT. The range of $\hat{f}_0$ is determined by the noise curves of the interferometers, likely detectable source frequencies [21], and limitations due to the increasing computational cost at high frequencies.

The range of $\dot{f}$ values searched is $[-1 \times 10^{-8}, 0]$ Hz s^{-1} for the StackSlide and PowerFlux methods and $[-2.2 \times 10^{-9}, 0]$ Hz s^{-1} for the Hough method. The ranges of $\dot{f}$ are determined by the computational cost, as
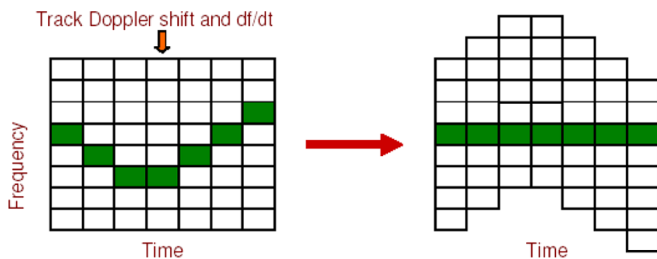

FIG. 2 (color online).   An illustration of the discrete frequency bins of the short Fourier transform (SFTs) of the data are shown vertically, with the discrete start times of the SFTs shown horizontally. The dark pixels represent a signal in the data. Its frequency changes with time due to Doppler shifts and intrinsic evolution of the source. By sliding the frequency bins, the power from a source can be lined up and summed after appropriate weighting or transformation. This is, in essence, the starting point for all of the semicoherent search methods presented here, though the actual implementations differ significantly.

well as by the low probability of finding an object with $|\dot{f}|$ higher than the values searched—in other words, the ranges of $\dot{f}$ are narrow enough to complete the search in a reasonable amount of time, yet wide enough to include likely signals. All known isolated pulsars spin down more slowly than the two values of $|\dot{f}|_{\text{max}}$ used here, and as seen in the results section, the ellipticity required for higher $|\dot{f}|$ is improbably high for a source losing rotational energy primarily via gravitational radiation at low frequencies. A small number of isolated pulsars in globular clusters exhibit slight spin-up, believed to arise from acceleration in the Earth's direction; such spin-up values have magnitudes small enough to be detectable with the zero-spin-down templates used in these searches, given a strong enough signal. The parameter ranges correspond to a minimum spin-down time scale $f/|4\dot{f}|$ (the gravitational-wave spin-down age) of 40 years for a source emitting at 50 Hz and 800 years for a source at 1000 Hz. Since for known pulsars [22] this characteristic time scale is at least hundreds of years for frequencies on the low end of our range and tens of millions of years for frequencies on the high end, we see again that the ranges of $|\dot{f}|$ are wide enough to include sources from this population.

As discussed in our previous reports [6,7], the number of sky points that must be searched grows quadratically with the frequency $\hat{f}_0$, ranging here from about five thousand at 50 Hz to about 2×10^6 at 1000 Hz. All three methods use nearly isotropic grids which cover the entire sky. The PowerFlux search also divides the sky into regions according to susceptibility to stationary instrumental line artifacts. Sky grid and spin-down spacings and other details are provided below.

2. Upper limits

While the parameter space searched is similar for the three methods, there are important differences in the way upper limits are set. StackSlide and Hough both set population-based frequentist limits on h_0 by carrying out Monte Carlo simulations of a random population of pulsar sources distributed uniformly over the sky and with isotropically distributed spin axes. PowerFlux sets strict frequentist limits on circular and linear-polarization amplitudes $h_0^{\text{Circ-limit}}$ and $h_0^{\text{Lin-limit}}$, which correspond to limits on most and least favorable pulsar inclinations, respectively. The limits are placed separately on tiny patches of the sky, with the highest strain upper limits presented here. In this context "strict" means that, regardless of its polarization angle ψ or inclination angle ι, regardless of its sky location (within fiducial regions discussed below), and regardless of its frequency value and spin-down within the frequency and spin-down step sizes of the search template, an isolated pulsar of true strain amplitude $h_0 = 2h_0^{\text{Lin-limit}}$, would have yielded a higher measured amplitude than what we measure, in at least 95% of independent observations. The circular-

polarization limits $h_0^{\text{Circ-limit}}$ apply only to the most favorable inclinations ($\iota \approx 0, \pi$), regardless of sky location and regardless of frequency and spin-down, as above.

Because of these different upper-limit setting methods, sharp instrumental lines are also handled differently. StackSlide and Hough carry out removal of known instrumental lines of varying widths in individual SFTs. The measured powers in those bins are replaced with random noise generated to mimic the noise observed in neighboring bins. This line cleaning technique can lead to a true signal being missed because its apparent frequency may coincide with an instrumental line for a large number of SFTs. However, population-averaged upper limits are determined self-consistently to include loss of detection efficiency due to line removal, by using Monte Carlo simulations.

Since its limits are intended to be strict, that is, valid for any source inclination and for any source location within its fiducial area, PowerFlux must handle instrumental lines differently. Single-bin lines are flagged during data preparation so that when searching for a particular source an individual SFT bin power is ignored when it coincides with the source's apparent frequency. If more than 80% of otherwise eligible bins are excluded for this reason, no attempt is made to set a limit on strain power from that source. In practice, however, the 80% cutoff is not used because we have found that all such sources lie in certain unfavorable regions of the sky, which we call ''skybands'' and which we exclude when setting upper limits. These skybands depend on source frequency and its derivative, as described in Sec. V D 4.

3. Data preparation

Other differences among the methods concern the data windowing and filtering used in computing Fourier transforms and concern the noise estimation. StackSlide and Hough apply high pass filters to the data above 40 Hz, in addition to the filter used to produce the calibrated data stream, and use Tukey windowing. PowerFlux applies no additional filtering and uses Hann windowing with 50% overlap between adjacent SFT's. StackSlide and Hough use median-based noise floor tracking [23–25]. In contrast, Powerflux uses a time-frequency decomposition. Both of these noise estimation methods are described in Sec. V.

The raw, uncalibrated data channels containing the strain measurements from the three interferometers are converted to a calibrated ''$h(t)$'' data stream, following the procedure described in [26], using calibration reference functions described in [27]. SFTs are generated directly from the calibrated data stream, using 30-minute intervals of data for which the interferometer is operating in what is known as science-mode. The choice of 30 minutes is a trade-off between intrinsic sensitivity, which increases with SFT length, and robustness against frequency drift during the SFT interval due to the Earth's motion, source

spin-down, and nonstationarity of the data [7]. The requirement that each SFT contain contiguous data at nominal sensitivity introduces duty factor loss from edge effects, especially for the Livingston interferometer ($\simeq 20\%$) which had typically shorter contiguous-data stretches. In the end, the StackSlide and Hough searches used 1004 SFTs from H1 and 899 from L1, the two interferometers with the best broadband sensitivity. For PowerFlux, the corresponding numbers of overlapped SFTs were 1925 and 1628. The Hough search also used 1063 H2 SFTs. In each case, modest requirements were placed on data quality to avoid short periods with known electronic saturations, unmonitored calibration strengths, and the periods immediately preceding loss of optical cavity resonance.

B. Definitions and notation

Let N be the number of SFTs, T_{coh} the time-baseline of each SFT, and M the number of uniformly spaced data points in the time domain from which the SFT is constructed. If the time series is denoted by x_j ($j = 0, 1, 2 \ldots M - 1$), then our convention for the discrete Fourier transform is

$$\tilde{x}_k = \Delta t \sum_{j=0}^{M-1} x_j e^{-2\pi \text{i} jk/M}, \tag{12}$$

where $k = 0, 1, 2 \ldots (M - 1)$, and $\Delta t = T_{\text{coh}}/M$. For $0 \leq k \leq M/2$, the frequency index k corresponds to a physical frequency of $f_k = k/T_{\text{coh}}$.

In each method, the ''power'' (in units of spectral density) associated with frequency bin k and SFT i is taken to be

$$P_k^i = \frac{2|\tilde{x}_k^i|^2}{T_{\text{coh}}}. \tag{13}$$

It proves convenient to define a normalized power by

$$\rho_k^i = \frac{P_k^i}{S_k^i}. \tag{14}$$

The quantity S_k^i is the single-sided power spectral density of the detector noise at frequency f_k, the estimation of which is described below. Furthermore, a threshold, ρ_{th}, can be used to define a *binary count* by [10]:

$$n_k^i = \begin{cases} 1 & \text{if } \rho_k^i \geq \rho_{\text{th}} \\ 0 & \text{if } \rho_k^i < \rho_{\text{th}} \end{cases}. \tag{15}$$

When searching for a signal using template λ the detector antenna pattern and frequency of the signal are found at the midpoint time of the data used to generate each SFT. Frequency dependent quantities are then evaluated at a frequency index k corresponding to the bin nearest this

TABLE I. Summary of notation used.

Quantity	Description
P_i	Power for SFT i and template λ
ρ_i	Normalized power for SFT i and template λ
n_i	Binary count for SFT i and template λ
S_i	Power spect. noise density for SFT i and template λ
F_+^i	F_+ at midpoint of SFT i for template λ
$F_\times^i$	$F_\times$ at midpoint of SFT i for template λ

frequency. To simplify the equations in the rest of this paper we drop the frequency index k and use the notation given in Table I to define various quantities for SFT i and template λ.

C. Basic StackSlide, Hough, and PowerFlux formalism

We call the detection statistics used in this search the "StackSlide Power," P, the "Hough Number Count," n, and the "PowerFlux Signal Estimator," R. The basic definitions of these quantities are given below.

Here the simple StackSlide method described in [15] is used; the "StackSlide Power" for a given template is defined as

$$P = \frac{1}{N} \sum_{i=0}^{N-1} \rho_i. \tag{16}$$

This normalization results in values of P with a mean value of unity and, for Gaussian noise, a standard deviation of $1/\sqrt{N}$. Details about the value and statistics of P in the presence and absence of a signal are given in Appendix B and [15].

In the Hough search, instead of summing the normalized power, the final statistic used in this paper is a weighted sum of the binary counts, giving the "Hough number count":

$$n = \sum_{i=0}^{N-1} w_i n_i, \tag{17}$$

where the Hough weights are defined as

$$w_i \propto \frac{1}{S_i}\{(F_+^i)^2 + (F_\times^i)^2\}, \tag{18}$$

and the weight normalization is chosen according to

$$\sum_{i=0}^{N-1} w_i = N. \tag{19}$$

With this choice of normalization the Hough number count n lies within the range $[0, N]$. Thus, we take a binary count n_i to have greater weight if the SFT i has a lower noise floor and if, in the time interval corresponding to this SFT,

the beam-pattern functions are larger for a particular point in the sky. Note that the sensitivity of the search is governed by the ratios of the different weights, not by the choice of overall scale. In the next section we show that these weights maximize the sensitivity, averaged over the orientation of the source. This choice of w_i was originally derived in [16] using a different argument and is similar to that used in the PowerFlux circular-polarization projection described next. More about the Hough method is given in [7,10].

The PowerFlux method takes advantage of the fact that less weight should be given to times of greater noise variance or smaller detector antenna response to a signal. Noting that power estimated from the data divided by the antenna pattern increases the variance of the data at times of small detector response, the problem reduces to finding weights that minimize the variance, or in other words that maximize the signal-to-noise ratio. The resulting PowerFlux detection statistic is [17],

$$R = \frac{2}{T_{\text{coh}}} \frac{\sum_{i=0}^{N-1} W_i P_i/(F_\psi^i)^2}{\sum_{i=0}^{N-1} W_i}, \tag{20}$$

where the PowerFlux weights are defined as

$$W_i = [(F_\psi^i)^2]^2/S_i^2, \tag{21}$$

and where

$$(F_\psi^i)^2 = \begin{cases} (F_+^i)^2 & \text{linear polarization} \\ (F_+^i)^2 + (F_\times^i)^2 & \text{circular polarization} \end{cases}. \tag{22}$$

As noted previously, the PowerFlux method searches using four linear-polarization projections and one circular-polarization projection. For the linear-polarization projections, note that $(F_+^i)^2$ is evaluated at the angle ψ, which is the same as $(F_\times^i)^2$ evaluated at the angle $\psi - \pi/4$; for circular polarization, the value of $(F_+^i)^2 + (F_\times^i)^2$ is independent of ψ. Finally note that the factor of $2/T_{\text{coh}}$ in Eq. (20) makes R dimensionless and is chosen to make it directly related to an estimate of the squared amplitude of the signal for the given polarization. Thus R is also called in this paper the "PowerFlux signal estimator." (See [17] and Appendix A for further discussion.)

We have shown in Eqs. (16)–(22) how to compute the detection statistic (or signal estimator) for a given template. The next section gives the details of the implementation and pipelines used, where these quantities are calculated for a set of templates λ and analyzed.

V. IMPLEMENTATIONS AND PIPELINES

A. Running median-noise estimation

The implementations of the StackSlide and Hough methods described below use a "running median" to estimate the mean power and, from this estimate, the power

spectral density of the noise, for every frequency bin of every SFT. PowerFlux uses a different noise decomposition method described in its implementation section below.

Note that for Gaussian noise, the single-sided power spectral density can be estimated using

$$S_k^i \cong \frac{2\langle|\tilde{x}_k^i|^2\rangle}{T_{\text{coh}}}, \qquad (23)$$

where the angle brackets represent an ensemble average. The estimation of S_k^i must guard against any biases introduced by the presence of a possible signal and also against narrow spectral disturbances. For this reason the mean, $\langle|\tilde{x}_k^i|^2\rangle$, is estimated via the median. We assume that the noise is stationary within a single SFT, but allow for non-stationarities across different SFTs. In every SFT we calculate the "running median" of $|\tilde{x}_k^i|^2$ for every 101 frequency bins centered on the kth bin, and then estimate $\langle|\tilde{x}_k^i|^2\rangle$ [23–25] by dividing by the expected ratio of the median to the mean.

Note, however, that in the StackSlide search, after the estimated mean power is used to compute S_k^i in the denominator of Eq. (14) these terms are summed in Eq. (16), while the Hough search applies a cutoff to obtain binary counts in Eq. (15) before summing. This results in the use of a different correction to get the mean in the StackSlide search from that used in the Hough search. For a running median using 101 frequency bins, the effective ratio of the median to mean used in the StackSlide search was 0.691 162 (which was chosen to normalize the data so that the mean value of the StackSlide Power equals one) compared with the expected ratio for an exponential distribution of 0.698 073 used in the Hough search (which is explained in Appendix A of [7]). It is important to realize that the results reported here are valid independent of the factor used, since any overall constant scaling of the data does not affect the selection of outliers or the reported upper limits, which are based on Monte Carlo injections subjected to the same normalization.

B. The StackSlide implementation

1. Algorithm and parameter space

The StackSlide method uses power averaging to gain sensitivity by decreasing the variance of the noise [12–15]. Brady and Creighton [12] first described this approach in the context of gravitational-wave detection as a part of a hierarchical search for periodic sources. Their method consists of averaging the power from a demodulated time series, but as an approximation did not include the beam-pattern response of the detector. In Ref. [15], a simple implementation is described that averages the normalized power given in Eq. (14). Its extension to averaging the maximum likelihood statistic (known as the $\mathcal{F}$-statistic) which does include the beam-pattern response is men-

tioned in Ref. [15] (see also [6,10,18]), and further extensions of the StackSlide method are given in [13].

As noted above, the simple StackSlide method given in [15] is used here and the detection statistic, called the "StackSlide Power," is defined by Eq. (16). The normalization is chosen so that the mean value of P is equal to 1 and its standard deviation is $1/\sqrt{N}$ for Gaussian noise alone. For simplicity, the StackSlide Power signal-to-noise ratio (in general the value of P minus its mean value and then divided by the standard deviation of P) will be defined in this paper as $(P - 1)\sqrt{N}$, even for non-Gaussian noise.

The StackSlide code, which implements the method described above, is part of the C-based LSC Algorithms Library Applications (LALapps) stored in the LSCsoft CVS repository [20]. The code is run in a pipeline with options set to produce the results from a search and from Monte Carlo simulations. Parallel jobs are run on computer clusters within the LSC, in the Condor environment [28], and the final post processing steps are performed using Matlab [29]. The specific StackSlide pipeline used to find the upper limits presented in this paper is shown in Fig. 3. The first three boxes on the left side of the pipeline can also be used to output candidates for follow-up searches.

A separate search was run for each successive 0.25 Hz band within 50–1000 Hz. The spacing in frequency used is given by Eq. (11). The spacing in $\dot{f}$ was chosen as that which changes the frequency by one SFT frequency bin during the observation time T_{obs}, i.e., so that $\dot{f}T_{\text{obs}} = \delta f$. For simplicity $T_{\text{obs}} = 2.778 \times 10^6$ seconds $\simeq 32.15$ days was chosen, which is greater than or equal to T_{obs} for each interferometer. Thus, the $\dot{f}$ part of the parameter space was over-covered by choosing
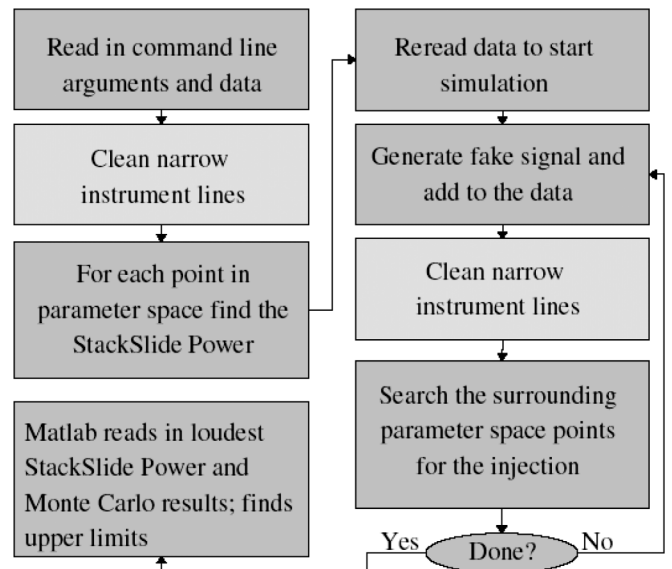

FIG. 3. Flow chart for the pipeline used to find the upper limits presented in this paper using the StackSlide method.

$$|\delta\dot{f}| = \frac{\delta f}{T_{\mathrm{obs}}} = \frac{1}{T_{\mathrm{coh}}T_{\mathrm{obs}}} = 2 \times 10^{-10}\ \mathrm{Hz\,s}^{-1}. \quad (24)$$

Values of $\dot{f}$ in the range $[-1 \times 10^{-8}\ \mathrm{Hz\,s}^{-1}, 0\ \mathrm{Hz\,s}^{-1}]$ were searched. This range corresponds to a search over 51 values of $\dot{f}$, which is the same as PowerFlux used in its low-frequency search (discussed in Sec. V D).

The sky grid used is similar to that used for the all-sky search in [6], but with a spacing between sky-grid points appropriate for the StackSlide search. This grid is isotropic on the celestial sphere, with an angular spacing between points chosen for the 50–225 Hz band, such that the maximum change in Doppler shift from one sky-grid point to the next would shift the frequency by half a bin. This is given by

$$\delta\theta_0 = \frac{0.5c\,\delta f}{\hat{f}(v\sin\theta)_{\mathrm{max}}} = 9.3 \times 10^{-3}\ \mathrm{rad}\left(\frac{300\ \mathrm{Hz}}{\hat{f}}\right), \quad (25)$$

where v is the magnitude of the velocity **v** of the detector in the SSB frame, and θ is the angle between **v** and the unit vector $\hat{\mathbf{n}}$ giving the sky position of the source. Equations (24) and (25) are the same as Eqs. (19) and (22) in [7], which represent conservative choices that over-cover the parameter space. Thus, the parameter space used here corresponds to that in Ref. [7], adjusted to the S4 observation time, and with the exception that a stereographic projection of the sky is not used. Rather an isotropic sky grid is used like the one used in [6].

One difficulty is that the computational cost of the search increases quadratically with frequency, due to the increasing number of points on the sky grid. To reduce the computational time, the sky-grid spacing given in Eq. (25) was increased by a factor of 5 above 225 Hz. This represents a savings of a factor of 25 in computational cost. It was shown through a series of simulations, comparing the upper limits in various frequency bands with and without the factor of 5 increase in grid spacing, that this changes the upper limits on average by less than 0.3%, with a standard deviation of 2%. Thus, this factor of 5 increase was used to allow the searches in the 225–1000 Hz band to complete in a reasonable amount of time.

It is not surprising that the sky-grid spacing can be increased, for at least three reasons. First, the value for $\delta\theta_0$ given in Eq. (25) applies to only a small annular region on the sky, and is smaller than the average change. Second, only the net change in Doppler shift during the observation time is important, which is less than the maximum Doppler shift due to the Earth's orbital motion during a one month run. (If the Doppler shift were constant during the entire observation time, one would not need to search sky positions even if the Doppler shift varied across the sky. A source frequency would be shifted by a constant amount during the observation, and would be detected, albeit in a frequency bin different from that at the SSB.) Third, because of correlations on the sky, one can detect a signal

with negligible loss of SNR much farther from its sky location than the spacing above suggests.

2. Line cleaning

Coherent instrumental lines exist in the data which can mimic a continuous gravitational-wave signal for parameter-space points that correspond to little Doppler modulation. Very narrow instrumental lines are removed ("cleaned") from the data. In the StackSlide search, a line is considered "narrow" if its full width is less than 5% of the 0.25 Hz band, or less than 0.0125 Hz. The line must also have been identified *a priori* as a known instrument artifact. Known lines with less than this width were cleaned by replacing the contents of bins corresponding to lines with random values generated by using the running median to find the mean power using 101 bins from either side of the lines. This method is also used to estimate the noise, as described in Sec. V A.

It was found when characterizing the data that a comb of narrow 1 Hz harmonics existed in the H1 and L1 data, as shown in Fig. 4. Table II shows the lines cleaned during the StackSlide search. As the table shows, only this comb of narrow 1 Hz harmonics and injected lines used for calibration were removed. As an example of the cleaning process, Fig. 5 shows the amplitude spectral density estimated from 10 SFTs before and after line cleaning, for the band with the 1 Hz line at 150 Hz.

The cleaning of very narrow lines has a negligible effect on the efficiency to detect signals. Very broad lines, on the other hand, cannot be handled in this way. Bands with very broad lines were searched without any line cleaning. There
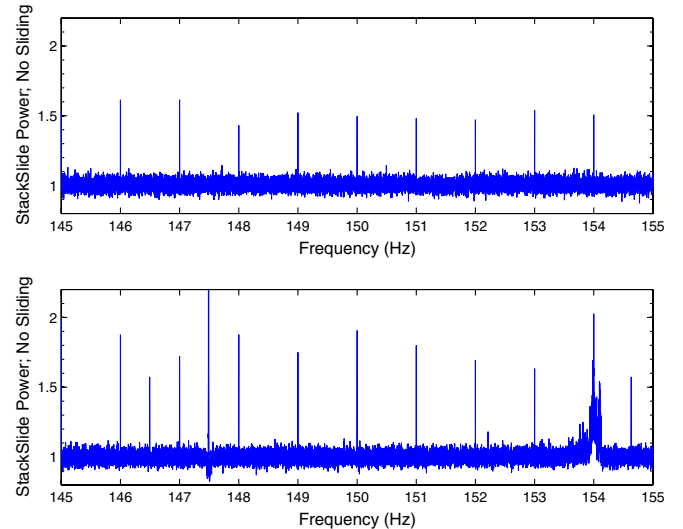

FIG. 4 (color online). The StackSlide Power for the 145–155 Hz band with no sliding. Harmonics of 1 Hz instrumental lines are clearly seen in H1 (top) and L1 (bottom). These lines are removed from the data by the StackSlide and Hough searches using the method described in the text, while PowerFlux search tracks these lines and avoids them when setting upper limits.

were also a number of highly disturbed bands, dominated either by the harmonics of 60 Hz power lines or by the violin modes of the suspended optics, that were excluded from the StackSlide results. (Violin modes refer to resonant

TABLE II. Instrumental lines cleaned during the StackSlide search. The frequencies cleaned are found by starting with that given in the second column, and then taking steps in frequency given in the third column, repeating this the number of times shown in the fourth column; the fifth and sixth columns show how many additional Hz are cleaned to the immediate left and right of each line.

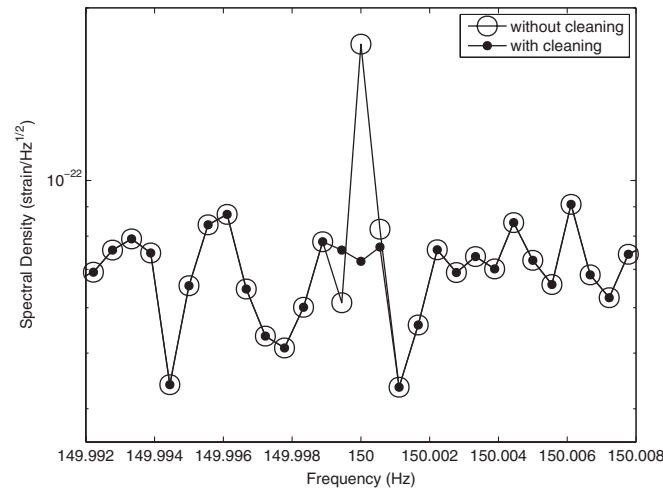| IFO	f_{start} (Hz)	f_{step} (Hz)	Num.	Δf_{left} (Hz)	Δf_{right} (Hz)	Description
H1	46.7	—	1	0.0	0.0	Cal. Line
H1	393.1	—	1	0.0	0.0	Cal. Line
H1	973.3	—	1	0.0	0.0	Cal. Line
H1	1144.3	—	1	0.0	0.0	Cal. Line
H1	0.0	1.0	1500	0.0006	0.0006	1 Hz Comb
L1	54.7	—	1	0.0	0.0	Cal. Line
L1	396.7	—	1	0.0	0.0	Cal. Line
L1	1151.5	—	1	0.0	0.0	Cal. Line
L1	0.0	1.0	1500	0.0006	0.0006	1 Hz Comb

FIG. 5. The L1 amplitude spectral density in a narrow frequency band estimated from 10 SFTs before and after the line cleaning used by the StackSlide pipeline. In the band shown, the 150 Hz bin, and one bin on either side of this bin have been replaced with estimates of the noise based on neighboring bins.

TABLE III. Frequency bands excluded from the StackSlide search.

Excluded Bands (Hz)	Description
[57, 63)	Power lines
[n60 − 1, n60 + 1) n = 2 to 16	Power line harmonics
[340, 350)	Violin modes
[685, 690)	Violin mode harmonics
[693, 696)	Violin mode harmonics

excitations of the steel wires that support the interferometer mirrors.) These are shown in Table III. While these bands can be covered by adjusting the parameters used to find outliers and set upper limits, we will wait for future runs to do this.

3. Upper limits method

After the lines are cleaned, the powers in the SFTs are normalized and the parameter space searched, with each template producing a value of the StackSlide Power, defined in Eq. (16). For this paper, only the "loudest" StackSlide Power is kept, resulting in a value P_{max} for each 0.25 Hz band, and these are used to set upper limits on the gravitational-wave amplitude, h_0. (The loudest coincident outliers are also identified, but none survive as candidates after follow-up studies described in Sec. VII A 1.) The upper limits are found by a series of Monte Carlo simulations, in which signals are injected in software with a fixed value for h_0, but with otherwise randomly chosen parameters, and the parameter-space points that surround the injection are searched. The number of times the loudest StackSlide Power found during the Monte Carlo simulations is greater than or equal to P_{max} is recorded, and this is repeated for a series of h_0 values. The 95% confidence upper limit is defined to be the value of h_0 that results in a detected StackSlide Power greater than or equal to P_{max} 95% of the time. As shown in Fig. 3, the line cleaning described above is done after each injection is added to the input data, which folds any loss of detection efficiency due to line cleaning into the upper limits self-consistently.

Figure 6 shows the measured confidence versus h_0 for an example frequency band. The upper-limit finding process
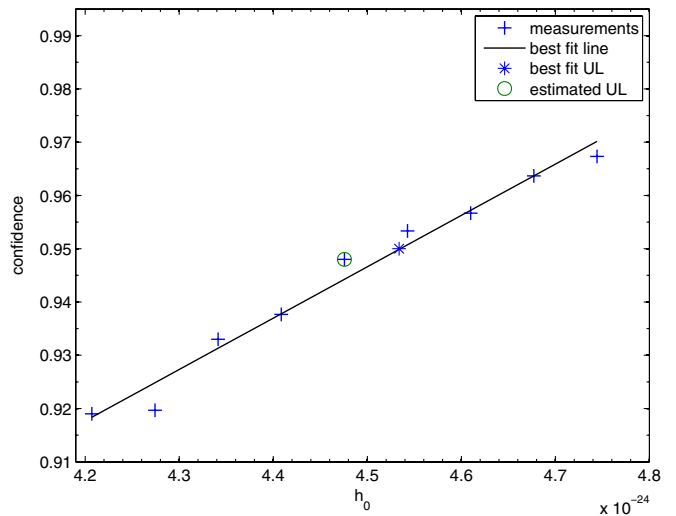

FIG. 6 (color online). Measured confidence vs h_0 for an example band (140–140.25 Hz in H1). A best-fit straight line is used to find the value of h_0 corresponding to 95% confidence and to estimate the uncertainties in the results (see text).

involves first making an initial guess of its value, then refining this guess using a single set of injections to find an estimate of the upper limit, and finally using this estimate to run several sets of injections to find the final value of the upper limit. These steps are now described in detail.

To start the upper-limit finding process, first an initial guess, h_0^{guess}, is used as the gravitational-wave amplitude. The initial guess need not be near the sought-after upper limit, just sufficiently large, as explained below. A single set of n injections is done (specifically $n = 3000$ was used) with random sky positions and isotropically distributed spin axes, but all with amplitude h_0^{guess}. The output list of StackSlide Powers from this set of injections is sorted in ascending order and the $0.05n$th (specifically for $n = 3000$ the 150th) smallest value of the StackSlide Power is found, which we call $P_{0.05}$. Note that the goal is to find the value of h_0 that makes $P_{0.05} = P_{\text{max}}$, so that 95% of the output powers are greater than the maximum power found during the search. This is what we call the 95% confidence upper limit. Of course, in general $P_{0.05}$ will not equal P_{max} unless our first guess was very lucky. However, as per the discussion concerning Eq. (B5), $P - 1$ is proportional to h_0^2 (i.e., removing the mean value due to noise leaves on average the power due to the presence of a signal). Thus, an estimate of the 95% h_0 confidence upper limits is given by the following rescaling of h_0^{guess},

$$h_0^{\text{est}} = \frac{\sqrt{P_{\text{max}} - 1}}{\sqrt{P_{0.05} - 1}} h_0^{\text{guess}}. \qquad (26)$$

Thus an estimated upper limit, h_0^{est}, is found from a single set of injections with amplitude h_0^{guess}; the only requirement is that h_0^{guess} is chosen loud enough to make $P_{0.05} > 1$.

It is found that using Eq. (26) results in an estimate of the upper limit that is typically within 10% of the final value. For example, the estimated upper limit found in this way is indicated by the circled point in Fig. 6. The value of h_0^{est} then becomes the first value for h_0 in a series of Monte Carlo simulations, each with 3000 injections, which use this value and 8 neighboring values, measuring the confidence each time. The Matlab [29] polyfit and polyval functions are then used to find the best-fit straight line to determine the value of h_0 corresponding to 95% confidence and to estimate the uncertainties in the results. This is the final step of the pipeline shown in Fig. 3.

C. The Hough transform implementation

1. Description of algorithm

The Hough transform is a general method for pattern recognition, invented originally to analyze bubble chamber pictures from CERN [30,31]; it has found many applications in the analysis of digital images [32]. This method has already been used to analyze data from the second science run (S2) of the LIGO detectors [7] and a detailed description can be found in [10]. Here we present only a brief

description, emphasizing the differences between the previous S2 search and the S4 search described here.

The Hough search uses a weighted sum of the binary counts as its final statistic, as given by Eqs. (15) and (19). In the standard Hough search as presented in [7,10], the weights are all set to unity. The weighted Hough transform was originally discussed in [16]. The software for performing the Hough transform has been adapted to use arbitrary weights without any significant loss in computational efficiency. Furthermore, the robustness of the Hough transform method in the presence of strong transient disturbances is not compromised by using weights because each SFT contributes at most w_i (which is of order unity) to the final number count.

The following statements can be proven using the methods of [10]. The mean number count in the absence of a signal is $\bar{n} = Np$, where N is the number of SFTs and p is the probability that the normalized power, of a given frequency bin and SFT defined by Eq. (14), exceeds a threshold ρ_{th}, i.e., p is the probability that a frequency bin is selected in the absence of a signal. For unity weighting, the standard deviation is simply $\sigma = \sqrt{Np(1 - p)}$. However, with more general weighting, it can be shown that σ is given by

$$\sigma = \sqrt{||\mathbf{w}||^2 p(1 - p)}, \qquad (27)$$

where $||\mathbf{w}||^2 = \sum_{i=0}^{N-1} w_i^2$. A threshold n_{th} on the number count corresponding to a false-alarm rate α_{H} is given by

$$n_{\text{th}} = Np + \sqrt{2||\mathbf{w}||^2 p(1 - p)}\text{erfc}^{-1}(2\alpha_{\text{H}}). \qquad (28)$$

Therefore n_{th} depends on the weights of the corresponding template λ. In this case, the natural detection statistic is not the "Hough number count" n, but the *significance* of a number count, defined by

$$s = \frac{n - \bar{n}}{\sigma}, \qquad (29)$$

where $\bar{n}$ and σ are the expected mean and standard deviation for pure noise. Values of s can be compared directly across different templates characterized by differing weight distributions.

The threshold ρ_{th} (c.f. Eq. (15)) is selected to give the minimum false-dismissal probability β_{H} for a given false-alarm rate. In [7] it was shown that the optimal choice for ρ_{th} is 1.6 which corresponds to a peak selection probability $p = e^{-\rho_{\text{th}}} \approx 0.2$. It can be shown that the optimal choice is unchanged by the weights and hence $\rho_{\text{th}} = 1.6$ is used once more [33].

Consider a population of sources located at a given point in the sky, but having uniformly distributed spin axis directions. For a template that is perfectly matched in frequency, spin-down, and sky position, and given the optimal peak selection threshold, it can be shown [33] that the weakest signal that can cross the threshold n_{th}

with a false-dismissal probability β_H has an amplitude

$$h_0 = 3.38 \mathcal{S}^{1/2} \left(\frac{||\mathbf{w}||}{\mathbf{w} \cdot \mathbf{X}} \right)^{1/2} \sqrt{\frac{1}{T_{\text{coh}}}}, \qquad (30)$$

where

$$\mathcal{S} = \text{erfc}^{-1}(2\alpha_H) + \text{erfc}^{-1}(2\beta_H), \qquad (31)$$

$$X_i = \frac{1}{S_i} \{ (F_+^i)^2 + (F_\times^i)^2 \}. \qquad (32)$$

As before, F_+^i and $F_\times^i$ are the values of the beam-pattern functions at the midpoint of the ith SFT. To derive (30) we have assumed that the number of SFTs N is sufficiently large and that the signal is weak [10].

From (30) it is clear that the scaling of the weights does not matter; $w_i \rightarrow k w_i$ leaves h_0 unchanged for any constant k. More importantly, it is also clear that the sensitivity is best, i.e. h_0 is minimum, when $\mathbf{w} \cdot \mathbf{X}$ is maximum:

$$w_i \propto X_i. \qquad (33)$$

This result is equivalent to Eq. (18).

In addition to improving sensitivity in single-interferometer analysis, the weighted Hough method allows automatic optimal combination of Hough counts from multiple interferometers of differing sensitivities.

Ideally, to obtain the maximum increase in sensitivity, we should calculate the weights for each sky location separately. In practice, we break up the sky into smaller patches and calculate one weight for each sky-patch center. The gain from using the weights will be reduced if the sky patches are too large. From Eq. (32), it is clear that the dependence of the weights on the sky position is only through the beam-pattern functions. Therefore, the sky patch size is determined by the typical angular scale over which F_+ and $F_\times$ vary; thus for a spherical detector using the beam-pattern weights would not gain us any sensitivity. For the LIGO interferometers, we have investigated this issue with Monte Carlo simulations using random Gaussian noise. Signals are injected in this noise corresponding to the H1 interferometer at a sky location (α_0, δ_0), while the weights are calculated at a mismatched sky position $(\alpha_0 + \delta\theta, \delta_0 + \delta\theta)$. The significance values are compared with the significance when no weights are used. An example of such a study is shown in Fig. 7. Here, we have injected a signal at $\alpha = \delta = 0$, $\cos\iota = 0.5$, zero spin-down, $\Phi_0 = \psi = 0$, and a signal-to-noise ratio corresponding approximately to a 6-σ level without weights. The figure shows a gain of $\sim 10\%$ at $\delta\theta = 0$, decreasing to zero at $\delta\theta \approx 0.3$ rad. We get qualitatively similar results for other sky locations, independent of frequency and other parameters. There is an additional gain due to the nonstationarity of the noise itself, which depends, however, on the quality of the data. In practice, we have chosen to break the sky up into 92 rectangular patches in which the average sky patch size is about 0.4 rad wide, corresponding to a
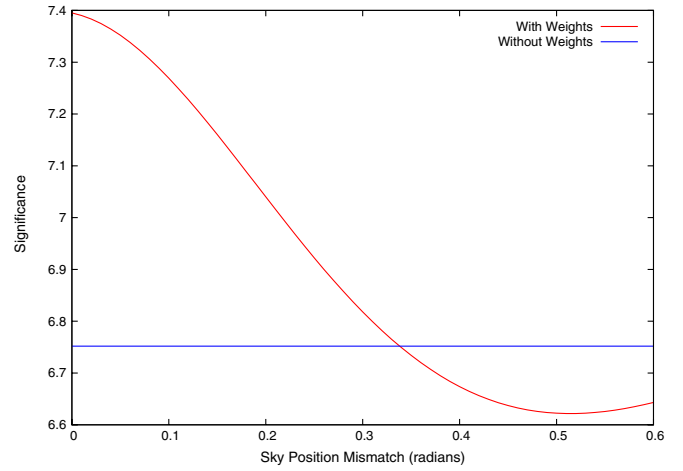

FIG. 7 (color online). The improvement in the significance as a function of the mismatch in the sky position. A signal is injected in fake noise at $\alpha = \delta = 0$ and the weights are calculated at $\alpha = \delta = \delta\theta$. The curve is the observed significance as a function of $\delta\theta$ while the horizontal line is the observed significance when no weights are used. See main text for more details.

maximum sky-position mismatch of $\delta\theta = 0.2$ rad in Fig. 7.

2. The Hough pipeline

The Hough analysis pipeline for the search and for setting upper limits follows roughly the same scheme as in [7]. In this section we present a short description of the pipeline, mostly emphasizing the differences from [7] and from the StackSlide and PowerFlux searches. As discussed in the previous subsection, the key differences from the S2 analysis [7] are (i) using the beam-pattern and noise weights, and (ii) using SFTs from multiple interferometers.

The total frequency range analyzed is 50–1000 Hz, with a resolution $\delta f = 1/T_{\text{coh}}$ as in (11). The resolution in $\dot{f}$ is 2.2×10^{-10} Hz s^{-1} given in (24), and the reference time for defining the spin-down is the start time of the observation. However, unlike StackSlide and PowerFlux, the Hough search is carried out over only 11 values of $\dot{f}$, including zero, in the range $[-2.2 \times 10^{-9}$ Hz s^{-1}, 0 Hz s$^{-1}]$. This choice is driven by the technical design of the current implementation, which uses look-up tables and partial Hough maps as in [7]. This implementation of the Hough algorithm is efficient when analyzing all resolvable points in $\dot{f}$, as given in (24), but this approach is incompatible with the larger $\dot{f}$ step sizes used in the other search methods, which permit those searches to search a larger $\dot{f}$ range for comparable computational cost.

The sky resolution is similar to that used by the StackSlide method for $f < 225$ Hz as given by (25). At frequencies higher than this, the StackSlide sky resolution is 5 times coarser, thus the Hough search is analyzing about 25 more templates at a given frequency and spin-down value. In each of the 92 sky patches, by means of the
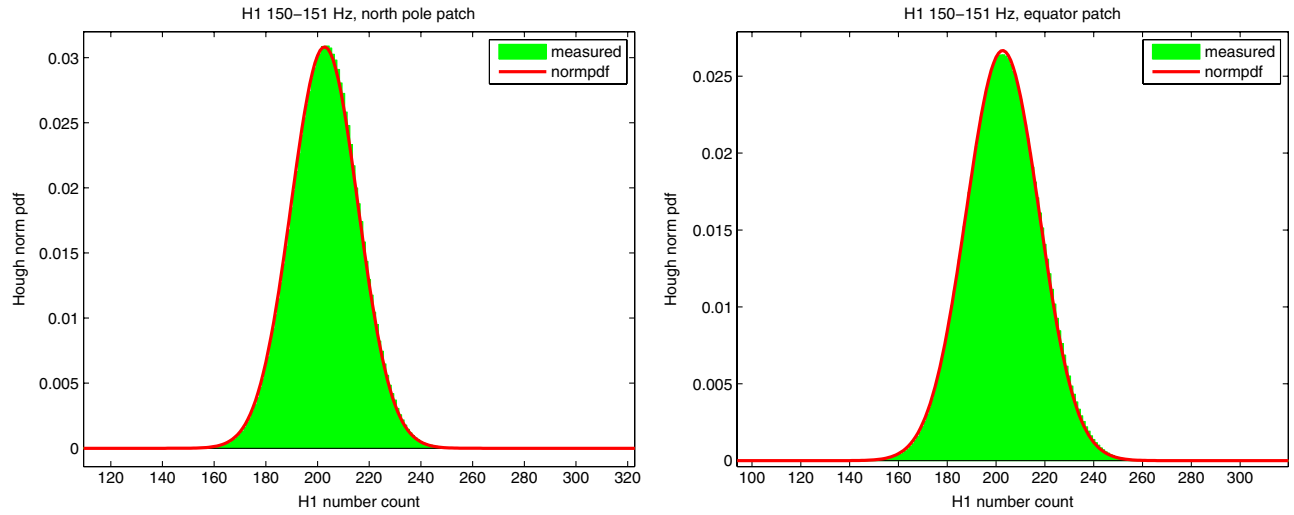
FIG. 8 (color online).   Two example histograms of the normalized Hough number count compared to a Gaussian distribution for the H1 detector in the frequency band 150–151 Hz. The left figure corresponds to a patch located at the north pole for the case in which the weights are used. The number of templates analyzed in this 1 Hz band is of 11×10^6, the number of SFTs 1004, the corresponding mean $\bar{n} = 202.7$, and $\sigma = 12.94$ is obtained from the weights. The right figure corresponds to a patch at the equator using the same data. In this case the number of templates analyzed in this 1 Hz band is of 10.5×10^6, and its corresponding $\sigma = 14.96$.

stereographic projection, the sky patch is mapped to a two-dimensional plane with a uniform grid of that resolution $\delta\theta_0$. Sky patches slightly overlap to avoid gaps among them (see [7] for further details).

Figure 8 shows examples of histograms of the number counts in two particular sky patches for the H1 detector in the 150–151 Hz band. In all the bands free of instrumental disturbances, the Hough number count distributions follows the expected theoretical distribution, which can be approximated by a Gaussian distribution. Since the number of SFTs for H1 is 1004, the corresponding mean $\bar{n} = 202.7$ and the standard deviation is given by Eq. (27). The standard deviation is computed from the weights **w** and varies among different sky patches because of varying antenna pattern functions.

The upper limits on h_0 are derived from the *loudest event*, registered over the entire sky and spin-down range in each 0.25 Hz band, not from the highest number count.

As for the StackSlide method, we use a frequentist method, where upper limits refer to a hypothetical population of isolated spinning neutron stars which are uniformly distributed in the sky and have a spin-down rate $\dot{f}$ uniformly distributed in the range $[-2.2 \times 10^{-9} \ \mathrm{Hz\,s^{-1}}, 0 \ \mathrm{Hz\,s^{-1}}]$. We also assume uniform distributions for the parameters $\cos\iota \in [-1, 1]$, $\psi \in [0, 2\pi]$, and $\Phi_0 \in [0, 2\pi]$. The strategy for calculating the 95% upper limits is roughly the same scheme as in [7], except for the treatment of narrow instrumental lines.

Known spectral disturbances are removed from the SFTs in the same way as for the StackSlide search. The known spectral lines are, of course, also consistently removed after each signal injection when performing the Monte Carlo simulations to obtain the upper limits.

The narrow instrumental lines cleaned from the SFT data are the same ones cleaned during the StackSlide search shown in Table II, together with ones listed in

TABLE IV.   Instrumental lines cleaned during the Hough search that were not listed in Table II (see text).

IFO	f_{start} (Hz)	f_{step} (Hz)	n	Δf_{left} (Hz)	Δf_{right} (Hz)	Description
H1	392.365	—	1	0.01	0.01	Cal. SideBand
H1	393.835	—	1	0.01	0.01	Cal. SideBand
H2	54.1	—	1	0.0	0.0	Cal. Line
H2	407.3	—	1	0.0	0.0	Cal. Line
H2	1159.7	—	1	0.0	0.0	Cal. Line
H2	110.934	36.9787	4	0.02	0.02	37 Hz Oscillator
L1	154.6328	8.1386	110	0.01	0.01	8.14 Hz Comb
L1	0.0	36.8725	50	0.02	0.02	37 Hz Oscillator[a]

[a]These lines were removed only in the multi-interferometer search.

Table IV. The additional lines listed in Table IV are cleaned to prevent large artifacts in one instrument from increasing the false-alarm rate of the Hough multi-interferometer search. Note that the L1 36.8725 Hz comb was eliminated midway through the S4 run by replacing a synthesized radio frequency oscillator for phase modulation with a crystal oscillator, and these lines were not removed in the Hough L1 single-interferometer analysis.

No frequency bands have been excluded from the Hough search, although the upper limits reported on the bands shown in Table III, that are dominated by 60 Hz power line harmonics or violin modes of the suspended optics, did not always give satisfactory convergence to an upper limit. In a few of these very noisy bands, upper limits were set by extrapolation, instead of interpolation, of the Monte Carlo simulations. Therefore the results reported on those bands have larger error bars. No parameter tuning was performed on these disturbed bands to improve the upper limits.

D. The PowerFlux implementation

The PowerFlux method is a variant on the StackSlide method in which the contributions from each SFT are weighted by the inverse square of the average spectral power density in each band and weighted according to the antenna pattern sensitivity of the interferometer for each point searched on the sky. This weighting scheme
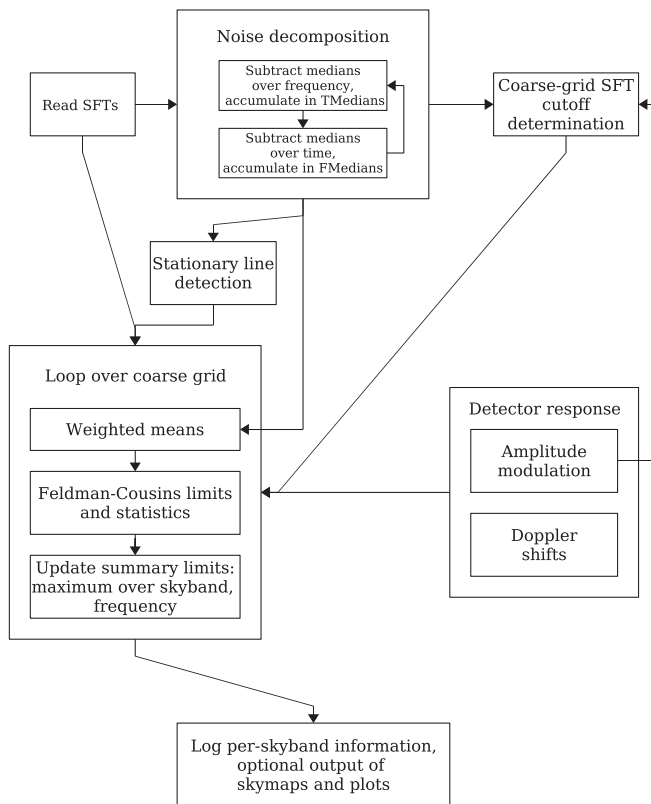

FIG. 9. Flow chart for the pipeline used to find the upper limits presented in this paper using the PowerFlux method.

has two advantages: (1) variance on the signal strength estimator is minimized, improving signal-to-noise ratio; and (2) the estimator is itself a direct measure of source strain power, allowing direct parameter estimation and dramatically reducing dependence on Monte Carlo simulations. Details of software usage and algorithms can be found in a technical document [17]. Figure 9 shows a flow chart of the algorithm, discussed in detail below.

1. Noise decomposition

Noise estimation is carried out through a time/frequency noise decomposition procedure in which the dominant variations are factorized within each nominal 0.25 Hz band as a product of a spectral variation and a time variation across the data run. Specifically, for each 0.25 Hz band, a matrix of logarithms of power measurements across the 0.56 mHz SFT bins and across the SFT's of the run is created. Two vectors, denoted TMedians and FMedians, are initially set to zero and then iteratively updated according to the following algorithm:

(1) For each SFT (row in matrix), the median value (logarithm of power) is computed and then added to the corresponding element of TMedians while subtracted from each matrix element in that row.

(2) For each frequency bin (column in matrix), the median value is computed and then added to the corresponding FMedians element, while subtracted from each matrix element in that column.

(3) The procedure repeats from step 1 until all medians computed in steps 1 and 2 are zero (or negligible).

The above algorithm typically converges quickly. The size of the frequency band treated increases with central frequency, as neighboring bins are included to allow for maximum and minimum Doppler shifts to be searched in the next step.

For stationary, Gaussian noise and for noise that follows the above assumptions of underlying factorized frequency and time dependence, the expected distribution of residual matrix values can be found from simulation. Figure 10 shows a sample expected residual power distribution following noise decomposition for simulated stationary, Gaussian data, along with a sample residual power distribution from the S4 data (0.25 Hz band of H1 near 575 Hz, in this case) following noise decomposition. The agreement in shape between these two distributions is very good and is typical of the S4 data, despite sometimes large variations in the corresponding TMedians and FMedians vectors, and despite, in this case, the presence of a moderately strong simulated pulsar signal (Pulsar2 in Table V).

The residuals are examined for outliers. If the largest residual value is found to lie above a threshold of 1.5, that corresponding 0.25 Hz band is flagged as containing a ''wandering line'' because a strong but drifting instrumental line can lead to such outliers. The value 1.5 is deter-
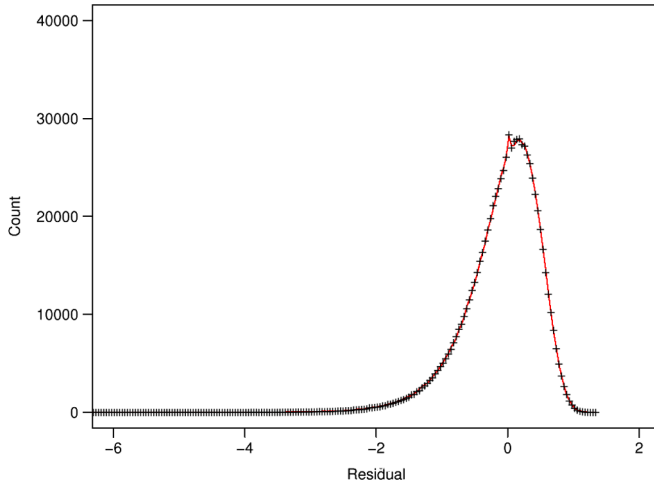
FIG. 10 (color online). Typical residual logarithmic power following noise decomposition for a sample 0.25 Hz band of H1 data (crosses) near 575 Hz in a band containing an injected pulsar. The residual is defined as the difference between a measured power for a given frequency bin in a given 30-minute period and the value predicted by the FMedians and TMedians vectors. The smooth curve is for a simulation in Gaussian noise.

mined empirically from Gaussian simulations. An extremely strong pulsar could also be flagged in this way, and indeed the strongest injected pulsars are labeled as wandering lines. Hence in the search, the wandering lines are followed up, but no upper limits are quoted here for the affected bands.

2. Line flagging

Sharp instrumental lines can prevent accurate noise estimation for pulsars that have detected frequencies in the same 0.56 mHz bin as the line. In addition, strong lines tend to degrade achievable sensitivity by adding excess apparent power in an affected search. In early LIGO sci-

ence runs, including the S4 run, there have been sharp instrumental lines at multiples of 1 Hz or 0.25 Hz, arising from artifacts in the data acquisition electronics.

To mitigate the most severe of these effects, the PowerFlux algorithm performs a simple line detection and flagging algorithm. For each 0.25 Hz band, the detected summed powers are ranked and an estimated Gaussian sigma computed from the difference in the 50% and 94% quantiles. Any bins with power greater than 5.0σ are marked for ignoring in subsequent processing. Specifically, when carrying out a search for a pulsar of a nominal true frequency, its contribution to the signal estimator is ignored when the detected frequency would lie in the same 0.56 mHz bin as a detected line. As discussed below, for certain frequencies, spin-downs, and points in the sky, the fraction of time a putative pulsar has a detected frequency in a bin containing an instrumental line can be quite large, requiring care. The deliberate ignoring of contributing bins affected by sharp instrumental lines does not lead to a bias in resulting limits, but it does degrade sensitivity, from loss of data. In any 0.25 Hz band, no more than five bins may be flagged as lines. Any band with more than five line candidates is examined manually.

3. Signal estimator

Once the noise decomposition is complete, with estimates of the spectral noise density for each SFT, the PowerFlux algorithm computes a weighted sum of the strain powers, where the weighting takes into account the underlying time and spectral variation contained in TMedians and FMedians and the antenna pattern sensitivity for an assumed sky location and incident wave polarization. Specifically, for an assumed polarization angle ψ and sky location, the following quantity is defined for each bin k of each SFT i:

TABLE V. Nominal (intended) parameters for hardware-injected signals, known as Pulsar0 to Pulsar11, for GPS reference time = 793 130 413 s (start of S4 run) at the SSB. These parameters are defined in Sec. III. As discussed in the text, imperfect calibration knowledge at the time of injections led to slightly different actual injected strain amplitudes among the three LIGO interferometers. The last two pulsars listed are binary system injections with additional orbital parameters not shown, which were injected during only the last day of the S4 run.

Name	f_0 (Hz)	df/dt (Hz s^{-1})	α (radians)	δ (radians)	ψ (radians)	A_+	$A_\times$
Pulsar0	265.576 933 18	-4.15×10^{-12}	1.248 816 734	$-0.981\,180\,225$	0.770 087 086	4.0250×10^{-25}	3.9212×10^{-25}
Pulsar1	849.070 861 08	-3.00×10^{-10}	0.652 645 832	$-0.514\,042\,406$	0.356 035 53	2.5762×10^{-24}	1.9667×10^{-24}
Pulsar2	575.163 567 32	-1.37×10^{-13}	3.756 928 84	0.060 108 958	$-0.221\,788\,475$	7.4832×10^{-24}	-7.4628×10^{-24}
Pulsar3	108.857 159 40	-1.46×10^{-17}	3.113 188 712	$-0.583\,578\,803$	0.444 280 306	1.6383×10^{-23}	-2.6260×10^{-24}
Pulsar4	1402.110 490 84	-2.54×10^{-08}	4.886 706 854	$-0.217\,583\,646$	$-0.647\,939\,117$	2.4564×10^{-22}	1.2652×10^{-22}
Pulsar5	52.808 324 36	-4.03×10^{-18}	5.281 831 296	$-1.463\,269\,033$	$-0.363\,953\,188$	5.8898×10^{-24}	4.4908×10^{-24}
Pulsar6	148.440 064 51	-6.73×10^{-09}	6.261 385 269	$-1.141\,840\,21$	0.470 984 879	1.4172×10^{-24}	-4.2565×10^{-25}
Pulsar7	1220.933 156 55	-1.12×10^{-09}	3.899 512 716	$-0.356\,930\,834$	0.512 322 887	1.0372×10^{-23}	9.9818×10^{-24}
Pulsar8	193.949 772 54	-8.65×10^{-09}	6.132 905 166	$-0.583\,263\,151$	0.170 470 927	1.5963×10^{-23}	2.3466×10^{-24}
Pulsar9	763.847 316 499	-1.45×10^{-17}	3.471 208 243	1.321 032 538	$-0.008\,560\,279$	5.6235×10^{-24}	-5.0340×10^{-24}
Pulsar10	501.238 967 14	-7.03×10^{-16}	3.113 188 712	$-0.583\,578\,803$	0.444 280 306	6.5532×10^{-23}	-1.0504×10^{-24}
Pulsar11	376.070 129 771	-4.2620×10^{-15}	6.132 905 166	$-0.583\,263\,151$	0.170 470 927	2.6213×10^{-22}	-4.2016×10^{-23}

$$Q_i = \frac{P_i}{(F_\psi^i)^2}, \qquad (34)$$

where F_ψ^i is the ψ-dependent antenna pattern for the sky location, defined in Eq. (22). (See also Appendix A.)

As in Sec. IV B, to simplify the notation we define $Q_i = P_i/(F_\psi^i)^2$ as the value of Q_i for SFT i and a given template λ.

For each individual SFT bin power measurement P_i, one expects an underlying exponential distribution, with a standard deviation equal to the mean, a statement that holds too for Q_i. To minimize the variance of a signal estimator based on a sum of these powers, each contribution is weighted by the inverse of the expected variance of the contribution. Specifically, we compute the following signal estimator:

$$R = \frac{2}{T_{\rm coh}} \left(\sum_i \frac{1}{(\bar{Q}_i)^2} \right)^{-1} \sum_i \frac{Q_i}{(\bar{Q}_i)^2}, \qquad (35)$$

$$= \frac{2}{T_{\rm coh}} \left(\sum_i \frac{[(F_\psi^i)^2]^2}{(\bar{P}_i)^2} \right)^{-1} \sum_i \frac{(F_\psi^i)^2 P_i}{(\bar{P}_i)^2}, \qquad (36)$$

where $\bar{P}_i$ and $\bar{Q}_i$ are the expected uncorrected and antenna-corrected powers of SFT i averaged over frequency. Since the antenna factor is constant in this average, $\bar{Q}_i = \bar{P}_i/(F_\psi^i)^2$. Furthermore, $\bar{P}_i$ is an estimate of the power spectral density of the noise. The replacement $\bar{P}_i \cong S_i$ gives Eq. (20).

Note that for a SFT i with low antenna pattern sensitivity $|F_\psi^i|$, the signal estimator receives a small contribution. Similarly, SFT's i for which ambient noise is high receive small contributions. Because computational time in the search grows linearly with the number of SFT's and because of large time variations in noise, it proves efficient to ignore SFT's with sky-dependent and polarization-dependent effective noise higher than a cutoff value. The cutoff procedure saves significant computing time, with negligible effect on search performance.

Specifically, the cutoff is computed as follows. Let σ_j be the *ordered* estimated standard deviations in noise, taken to be the ordered means of $\bar{Q}_i = \frac{1}{k_{\rm max}} \Sigma_k \bar{Q}_k^i$, where $k_{\rm max}$ is the number of frequency bins used in the search template. Define $j_{\rm opt}$ to be the index $j_{\rm max}$ for which the quantity $\frac{1}{j_{\rm max}} \sqrt{\Sigma_{j=1}^{j_{\rm max}} \sigma_j^2}$ is minimized. Only SFT's for which $\sigma_j < 2\sigma_{j_{\rm opt}}$ are used for signal estimation. In words, $j_{\rm opt}$ defines the last SFT that improves rather than degrades signal estimator variance in an unweighted mean. For the weighted mean used here, the effective noise contributions are allowed to be as high as twice the value found for $j_{\rm opt}$. The choice of $2\sigma_{j_{\rm opt}}$ is determined empirically.

The PowerFlux search sets strict, frequentist, all-sky 95% confidence-level upper limits on the flux of gravita-
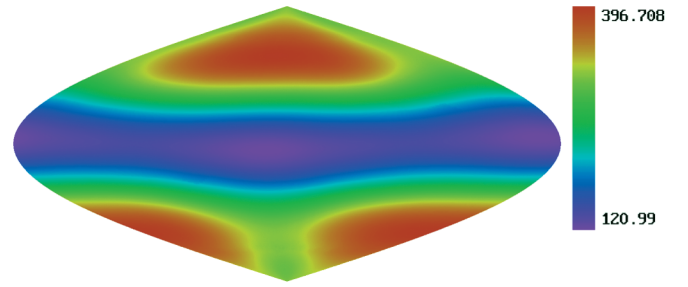

FIG. 11 (color). Sky map of run-summed PowerFlux weights for a 0.25 Hz band near 575 Hz for one choice of linear polarization in the S4 H1 data. The normalization corresponds roughly to the effective number of median-noise SFT's contributing to the sum.

tional radiation bathing the Earth. To be conservative in the strict limits, numerical corrections to the signal estimator are applied: (1) a factor of $1/\cos(\pi/8) = 1.082$ for maximum linear-polarization mismatch, based on twice the maximum half-angle of mismatch (see Appendix A); (2) a factor of 1.22 for bin-centered signal power loss due to Hann windowing (applied during SFT generation); and (3) a factor of 1.19 for drift of detected signal frequency across the width of the 0.56 mHz bins used in the SFT's. Note that the use of rectangular windowing would eliminate the need for correction (2) above, but would require a larger correction of 1.57 for (3).

Antenna pattern and noise weighting in the PowerFlux method allows weaker sources to be detected in certain regions of the sky, where run-averaged antenna patterns discriminate in declination and diurnal noise variations discriminate in right ascension. Figure 11 illustrates the resulting variation in effective noise across the sky for a 0.25 Hz H1 band near 575 Hz for the circular-polarization projection. By separately examining SNR, one may hope to detect a signal in a sensitive region of the sky with a strain significantly lower than suggested by the strict worst-case all-sky frequentist limits presented here, as discussed below in Sec. VI D. Searches are carried out for four linear polarizations, ranging over polarization angle from $\psi = 0$ to $\psi = \frac{3}{8}\pi$ in steps of $\pi/8$ and for (unique) circular polarization.

A useful computational savings comes from defining two different sky resolutions. A "coarse" sky gridding is used for setting the cutoff value defined above, while fine grid points are used for both frequency and amplitude demodulation. A typical ratio of number of coarse grid points to number of fine grid points used for Doppler corrections is 25.

4. Sky banding

Stationary and near-stationary instrumental spectral lines can be mistaken for a periodic source of gravitational radiation if the nominal source parameters are consistent with small variation in detected frequency during the time

of observation. The variation in the frequency at the detector can be found by taking the time derivative of Eq. (9), which gives

$$\frac{df}{dt} = \left(1 + \frac{\mathbf{v}(t) \cdot \hat{\mathbf{n}}}{c}\right)\dot{f} + \hat{f}(t)\frac{\mathbf{a}(t) \cdot \hat{\mathbf{n}}}{c}. \qquad (37)$$

The detector's acceleration **a** in this equation is dominated by the Earth's orbital acceleration $\mathbf{a}_{\text{Earth}}$, since the diurnal part of the detector's acceleration is small and approximately averages to zero during the observation. Thus, it should be emphasized that a single instrumental line can mimic sources with a range of slightly *different* frequencies and assumed different positions in the sky that lie in an annular band. For a source $\dot{f}$ assumed to be zero, the center of the band is defined by a circle 90 degrees away from the direction of the average acceleration of the Earth during the run where $\bar{\mathbf{a}}_{\text{Earth}} \cdot \hat{\mathbf{n}} = \mathbf{0}$, i.e., toward the average direction of the Sun during the run. For source spin-downs different from zero, there can be a large cancellation between assumed spin-down (or spin-up) and the Earth's average acceleration, leading to a shift of the annular region of apparent Doppler stationarity toward (away from) the Sun.

A figure of merit found to be useful for discriminating regions of "good" sky from "bad" sky (apparent detected frequency is highly stationary) is the "*S* parameter":

$$S = \dot{f} + [(\mathbf{\Omega} \times \mathbf{v}_{\text{Earth}}/c) \cdot \hat{\mathbf{n}}]\hat{f}_0, \qquad (38)$$

where $\mathbf{\Omega}$ is the Earth's angular velocity vector about the solar system barycenter. The term $\mathbf{\Omega} \times \mathbf{v}_{\text{Earth}}$ is a measure of the Earth's average acceleration during the run, where $\mathbf{v}_{\text{Earth}}$ is taken to be the noise-weighted velocity of the H1 detector during the run. Regions of sky with small $|S|$ for a given $\hat{f}$ and $\dot{f}$ have stationary detected frequency. As discussed below in Sec. VI D, such regions are not only prone to high false-alarm rates, but the line flagging procedure described in Sec. V D 2 leads to systematically underestimated signal strength and invalid upper limits. Hence limits are presented here for only sources with $|S|$ greater than a threshold value denoted S_{large}. The minimum acceptable value chosen for S_{large} is found from software signal injections to be 1.1×10^{-9} Hz s^{-1} for the 1-month S4 run and can be understood to be

$$S_{\text{large}} = \frac{N_{\text{occupied bins}}}{T_{\text{obs}} \cdot T_{\text{coh}}}, \qquad (39)$$

where $N_{\text{occupied bins}} \sim 5$ is the minimum total number of 0.56 mHz detection bins occupied by the source during the data run for reliable detection. In practice, we use still larger values for the H1 interferometer ($S_{\text{large}} = 1.85 \times 10^{-9}$ Hz s^{-1}) and L1 interferometer ($S_{\text{large}} = 3.08 \times 10^{-9}$ Hz s^{-1}) during the S4 run for the limits presented here because of a pervasive and strong comb of precise 1 Hz lines in both interferometers. These lines,
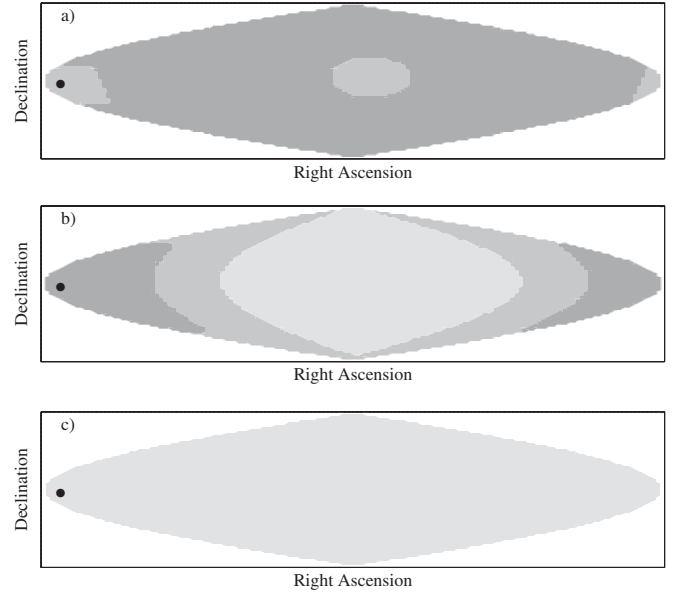

FIG. 12. S4 sky band regions (good—light gray, bad for L1—medium or dark gray, bad for H1 and L1—dark gray) for a source frequency $\hat{f} = 100$ Hz and three different assumed spin-down choices: (a) zero; (b) -3×10^{-9} Hz s^{-1}; and (c) -1×10^{-8} Hz s^{-1}. The black circle indicates the average position of the Sun during the data run.

caused by a global positioning system (GPS)-second synchronized electronic disturbance and worse in L1 than in H1, lead to high false-alarm rates from that data for lower values of S_{large}. For the frequency and spin-down ranges
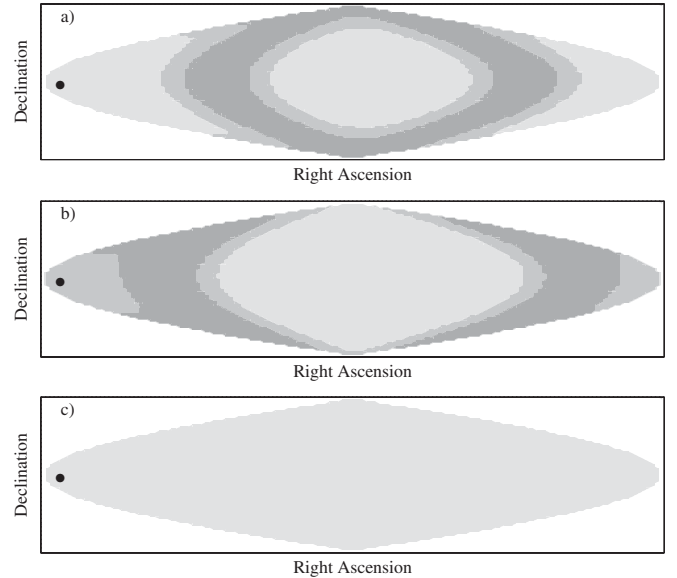

FIG. 13. S4 sky band regions (good—light gray, bad for L1—medium or dark gray, bad for H1 and L1—dark gray) for a source frequency $\hat{f} = 300$ Hz and three different assumed spin-down choices: (a) zero; (b) -3×10^{-9} Hz s^{-1}; and (c) -1×10^{-8} Hz s^{-1}. The black circle indicates the average position of the Sun during the data run.
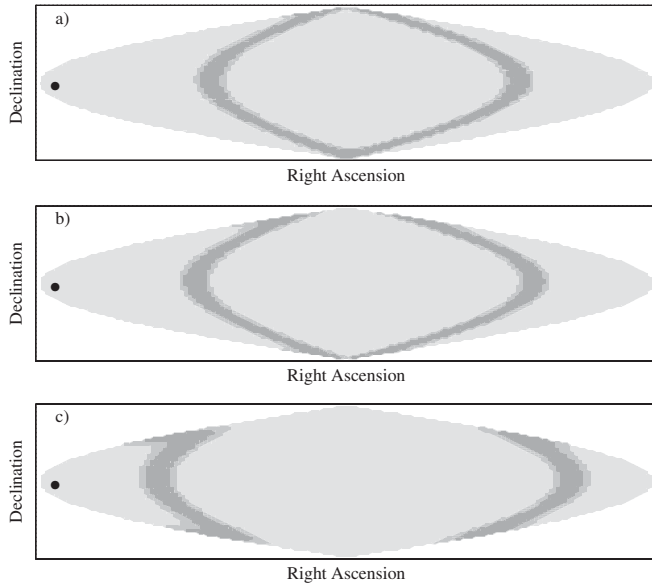
FIG. 14. S4 sky-band regions (good—light gray, bad for L1—medium or dark gray, bad for H1 and L1—dark gray) for a source frequency $\hat{f} = 1000$ Hz and three different assumed spin-down choices: (a) zero; (b) -3×10^{-9} Hz s^{-1}; and (c) -1×10^{-8} Hz s^{-1}. The black circle indicates the average position of the Sun during the data run.
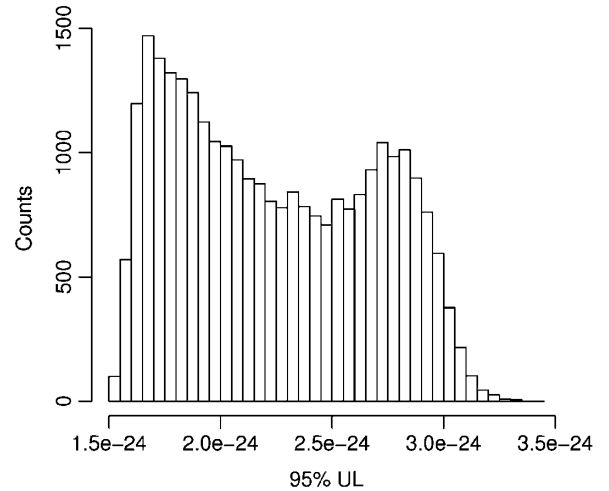

FIG. 15. Histogram of Feldman-Cousins 95% confidence-level upper limits in a 0.25 Hz band near 149 Hz in S4 H1 data. Each entry corresponds to the highest upper limit in the band for a single sky location.

searched in this analysis, the average fractions of sky lost to the sky band veto are 15% for H1 and 26% for L1.

Figures 12–14 illustrate the variation in the fraction of sky marked as bad as assumed source frequency and spin-down are varied. Generally, at low frequencies, large sky regions are affected, but only for low spin-down magnitude, while at high frequencies, small sky regions are affected, but the effects are appreciable to larger spin-down magnitude. It should be noted that the annular regions of the sky affected depend upon the start time and duration of a data run. The longer the data run, the smaller the region of sky for which Doppler stationarity is small. Future LIGO data runs of longer duration should have only small regions near the ecliptic poles for which stationary instrumental lines prove troublesome.

5. Grid-point upper limit determination

An intermediate step in the PowerFlux analysis is the setting of upper limits on signal strength for each sky point for each 0.56 mHz bin. The limits presented here for each interferometer are the highest of these intermediate limits for each 0.25 Hz band over the entire good sky. The intermediate limits are set under the assumption of Gaussian residuals in noise. In brief, for each 0.56 mHz bin and sky point, a Feldman-Cousins [34] 95% confidence level is set for an assumed normal distribution with a standard deviation determined robustly from quantiles of the entire 0.25 Hz band. The Feldman-Cousins approach provides the virtues of a well-behaved upper limit even

when background noise fluctuates well below its expectation value and of smooth transition between 1-sided and 2-sided limits, but in practice the highest upper limit for any 0.25 Hz band is invariably the highest measured power plus 1.96 times the estimated standard deviation on the background power for that bin, corresponding to a conventional *a priori* 1-sided 97.5% upper CL. A Kolmogorov-Smirnov (KS) statistic is computed to check the actual power against a Gaussian distribution for each 0.25 Hz band. Those bands that fail the KS test value of 0.07 ($> 5\sigma$ deviation for the S4 data sample) are flagged as "Non-Gaussian," and no upper limits on pulsars are quoted here for those bands, although a full search is carried out. Bands subject to violin modes and harmonics of the 60 Hz power mains tend to fail the KS test because of sharp spectral slope (and sometimes because nonstationarity of sharp features leads to poor noise factorization).

Figure 15 provides an example of derived upper limits from one narrow band. The figure shows the distribution of PowerFlux strain upper limits on linear-polarization amplitude h_0^{Lin} for a sample 0.25 Hz band of S4 H1 data near 149 Hz. The highest upper limit found is 3.35×10^{-24} (corresponding to a worst-case pulsar upper limit on h_0 of 6.70×10^{-24}). The bimodal distribution arises from different regions of the sky with intrinsically different antenna pattern sensitivities. The peak at 2.8×10^{-24} corresponds to points near the celestial equator where the run-averaged antenna pattern sensitivity is worst.

VI. HARDWARE INJECTIONS AND VALIDATION

All three methods discussed in this paper have undergone extensive internal testing and review. Besides individual unit tests of the software, hardware injections provided an end-to-end validation of the entire pipelines.

TABLE VI. Results of StackSlide analyses of the ten hardware-injected continuous gravitational-wave signals from isolated neutron stars.

	H1					L1				
Pulsar	Observed SNR	Injected SNR	Observed $\sqrt{P}$	Injected $\sqrt{P}$	Percent Difference	Observed SNR	Injected SNR	Observed $\sqrt{P}$	Injected $\sqrt{P}$	Percent Difference
Pulsar0	0.27	0.23	1.006	1.005	0.1%	0.15	0.13	1.003	1.003	0.1%
Pulsar1	1.62	0.80	1.035	1.017	1.7%	0.27	0.69	1.006	1.016	−1.0%
Pulsar2	8.92	8.67	1.179	1.175	0.4%	8.20	9.34	1.180	1.203	−1.9%
Pulsar3	199.78	174.72	3.124	2.943	6.2%	89.89	104.76	2.304	2.454	−6.1%
Pulsar4	2081.64	1872.24	9.607	9.116	5.4%	1279.12	1425.14	7.895	8.326	−5.2%
Pulsar5	0.05	1.30	1.001	1.028	−2.6%	1.02	0.44	1.024	1.010	1.4%
Pulsar6	0.17	2.94	1.004	1.063	−5.5%	2.90	1.36	1.067	1.032	3.4%
Pulsar7	6.25	5.50	1.129	1.114	1.3%	6.07	5.11	1.136	1.116	1.8%
Pulsar8	98.12	96.21	2.303	2.285	0.8%	92.77	103.45	2.334	2.441	−4.4%
Pulsar9	6.68	6.59	1.137	1.135	0.2%	2.61	3.69	1.061	1.085	−2.2%

The next subsections discuss the hardware injections, the validations of the three methods, and their pipelines. The detection of the hardware injections also shows in dramatic fashion that we can detect the extremely tiny signals that the detectors were designed to find.

A. Hardware injections

During a 15-day period in the S4 run, ten artificial isolated-pulsar signals were injected into all three LIGO interferometers at a variety of frequencies and time derivatives of the frequency, sky locations, and strengths. Two additional artificial binary pulsar signals were injected for approximately one day. These hardware injections were implemented by modulating the interferometer mirror positions via signals sent to voice actuation coils surrounding magnets glued to the mirror edges. The injections provided an end-to-end validation of the search pipelines. Table V summarizes the nominal parameters used in the isolated-pulsar injections; the parameters are defined in Sec. III.

Imperfect calibration knowledge at the time of these injections led to slightly different actual strain amplitude injections among the three LIGO interferometers. For the H1 and L1 comparisons between expected and detected signal strengths for these injections described in Sec. VI B, corrections must be applied for the differences from nominal amplitudes. The corrections are the ratios of the actuation function derived from final calibration to the actuation function assumed in the preliminary calibration used during the injections. For H1 this ratio was independent of the injection frequency and equal to 1.12. For L1, this ratio varied slightly with frequency, with a ratio of 1.11 for all injected pulsars except Pulsar1 (1.15) and Pulsar9 (1.18).

B. StackSlide validation

Besides individual unit tests and a review of each component of the StackSlide code, we have shown that simulated signals are detected with the expected StackSlide Power, including the hardware injections listed in Table V. Table VI shows the observed and injected SNR, and the square root of the observed and injected StackSlide Power, $\sqrt{P}$. The percent difference of the latter is given, since this compares amplitudes, which are easier to compare with calibration errors. The observed values were obtained by running the StackSlide code using a template that exactly matches the injection parameters, while the injected values were calculated using the parameters in Table V and the equations in Appendix B. The SNR's of Pulsar0, Pulsar1, Pulsar5, and Pulsar6 were too small to be detected, and Pulsar4 and Pulsar7 were out of the frequency band of the all-sky search. Pulsar2, Pulsar3, and Pulsar8 were detected as outliers with SNR > 7 (as discussed in Sec. VII) while Pulsar9 was not loud enough to pass this requirement. In all cases the observed StackSlide Power agrees well with that predicted, giving an end-to-end validation of the StackSlide code.
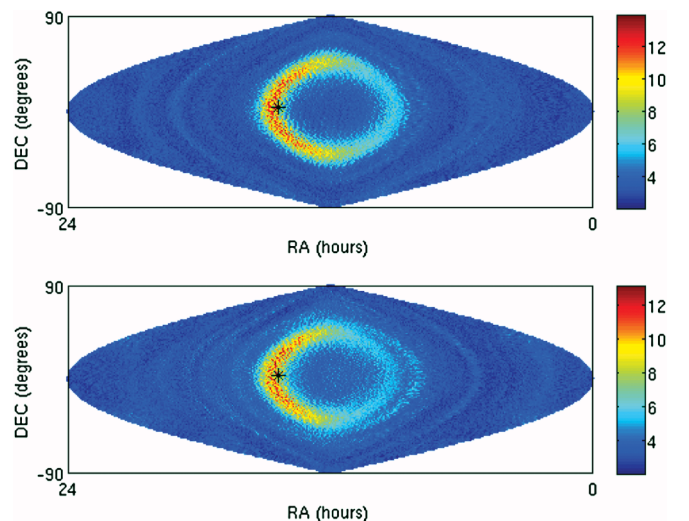

FIG. 16 (color). Detection of hardware-injected Pulsar 2 by the StackSlide code in the H1 (top) and L1 (bottom) data.

As an example of an all-sky search for a band with an injection, Fig. 16 shows the detection of Pulsar2 for a search of the H1 (top) and L1 (bottom) data, and only during the times the hardware injections were running. Later, when the entire S4 data set was analyzed Pulsar2 was still detected but with lower SNR, since this data includes times when the hardware injections were absent. Also note that, as explained in Sec. V D, because of strong correlations on the sky, a pulsar signal will be detected at many points that lie in an annular region in the sky that surrounds the point corresponding to the average orbital acceleration vector of the Earth, or its antipode. In fact, because of the large number of templates searched, random noise usually causes the maximum detected SNR to occur in a template other than the one which is closest to having the exact parameters of the signal. For example, for the exact template and times matching the Pulsar2 hardware injection, it was detected with SNR's of 8.92 and 8.20 in H1 and L1, respectively, as given in Table VI, while the largest SNR's shown in Fig. 16 are 13.84 and 13.29. During the search of the full data set (including times when Pulsar2 was off) it was detected with SNR 11.09 and 10.71 in H1 and L1, respectively.

C. Hough validation

Using the Hough search code, four hardware-injected signals have been clearly detected by analyzing the data from the interval when the injections took place. These correspond to Pulsar2, Pulsar3, Pulsar8, and Pulsar9. For each of these injected signals, a small-area search (0.4 rad $\times$ 0.4 rad) was performed, using a step size on the spin-down parameter of -4.2×10^{-10} Hz s^{-1}. Given the large spin-down value of Pulsar8 (-8.65×10^{-9} Hz s^{-1}), we have used 23 values of the spin-down spanning the range [-9.24×10^{-9} Hz s^{-1}, 0 Hz s^{-1}] to search for this pulsar. Because of its large amplitude, Pulsar8 can be detected even with a large mismatch in the spin-down value, although at the cost of lower SNR.

Figure 17 shows the significance maximized over different sky locations and spin-down values for the different frequencies. These four hardware-injected pulsars have been clearly detected, with the exception of Pulsar9 in the L1 data. Pulsar9 is marginally visible using the H1 data alone, with a maximum significance of 6.13, but when we combine the data from the three interferometers, the significance increases up to 8.32. Details are given in Table VII, including the frequency range of the detected signal, the frequency at which the maximum significance is obtained and its significance value.

Figure 18 shows the Hough significance maps for the multi-interferometer case. The maps displayed correspond either to the frequency and spin-down values nearest to the injected ones, or to those in which the maximum significance was observed. The location of the injected pulsars correspond to the center of each map. Note that the true
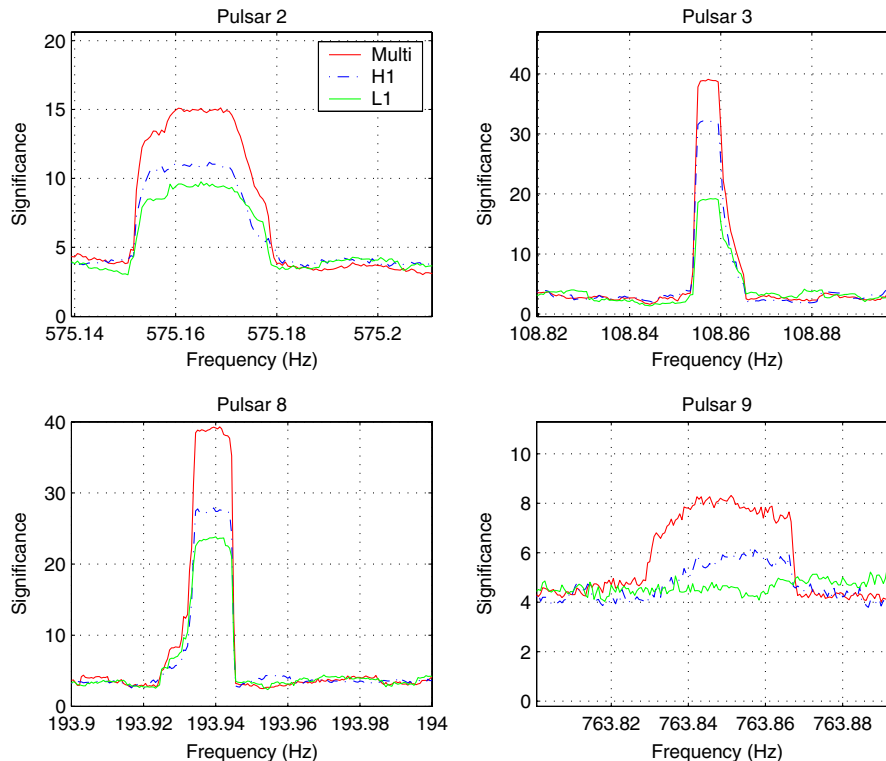

FIG. 17 (color online).   Maximum significance as a function of frequency corresponding to the multi-interferometer search (using the data from the three detectors) and the H1 and L1 alone.

TABLE VII.   Results of the Hough search for the hardware-injected signals for the multi-interferometer, H1 and L1 data.

Pulsar	Detector	f_0 range (Hz)	$f_0(max)$ (Hz)	Significance
Pulsar2	Multi-IFO	575.15–575.18	575.1689	15.1195
	H1	575.15–575.18	575.1667	11.1730
	L1	575.15–575.18	575.1650	9.7635
Pulsar3	Multi-IFO	108.855–108.86	108.8572	39.1000
	H1	108.855–108.86	108.8572	32.2274
	L1	108.855–108.86	108.8589	19.2267
Pulsar8	Multi-IFO	193.932–193.945	193.9411	39.2865
	H1	193.932–193.945	193.9394	27.9008
	L1	193.932–193.945	193.9400	23.8270
Pulsar9	Multi-IFO	763.83–763.87	763.8511	8.3159
	H1	763.83–763.87	763.8556	6.1268
	L1	—	—	5.4559

spin-down value of Pulsar8, -8.65×10^{-9} Hz s^{-1}, lies between the parameter values -8.82×10^{-9} Hz s^{-1} and -8.40×10^{-9} Hz s^{-1} of the nearest templates used.

D. PowerFlux validation

Several cross checks have been performed to validate the PowerFlux search algorithm. These validations range from simple and rapid Fourier-domain "power injections" to more precise time-domain software simulations, to hardware signal injections carried out during data taking.

Signal strain power injections have been carried out as part of PowerFlux algorithm development and for parameter tuning. These software injections involve superimposing calculated powers for assumed signals upon the LIGO power measurements and carrying out searches. For computational speed, when testing signal detection efficiency, only a small region of the sky around the known source direction is searched. A critical issue is whether the strict frequentist limits set by the algorithm are sufficiently conservative to avoid under-coverage of the intended frequent-
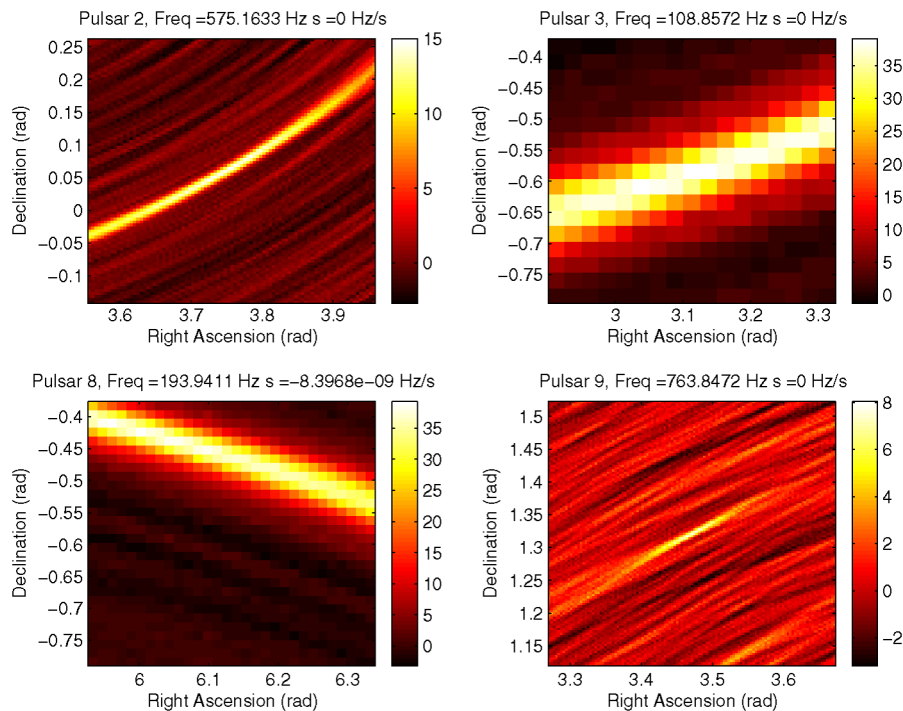

FIG. 18 (color online).   Maps of the Hough significance corresponding to the multi-interferometer case for Pulsar2, Pulsar3, Pulsar8, and Pulsar9. The location of the injected pulsars are the centers of the maps. For Pulsar2, Pulsar3, and Pulsar9, the maps correspond to the frequency and spin-down values closest to the real injected ones. For Pulsar8, we show the map containing the maximum significance value. The discrepancy in sky location is due to the mismatch in frequency and spin-down values between those used in the injections and those corresponding to the Hough map.
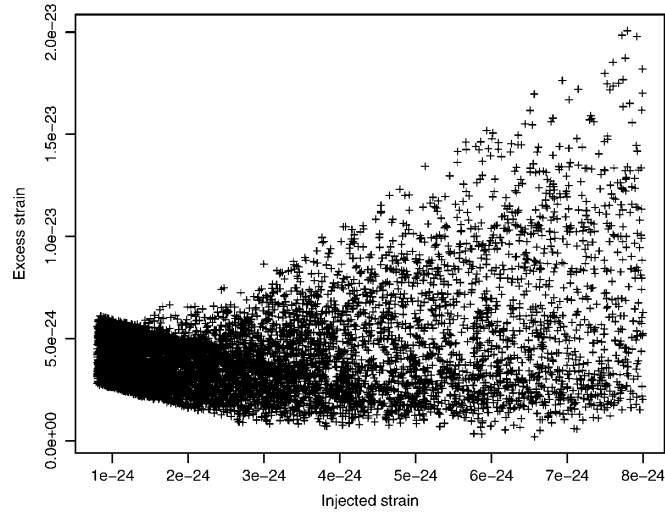
FIG. 19. Excess (upper limit minus injected) strain plotted vs injected signal strain for sample PowerFlux H1 elliptic-polarization near 140 Hz injections.

ist confidence band. We present here a set of figures that confirm over-coverage applies. Figure 19 shows the difference ("excess") between the Feldman-Cousins 95% confidence-level upper limit (conventional 97.5% upper limit) on strain and the injected strain for a sample of elliptic-polarization time-domain injections in the H1 interferometer for the 140.50–140.75 Hz band. Injection amplitudes were distributed logarithmically, while frequencies, spin-downs, sky locations, and orientations were distributed uniformly. One sees that there is indeed no under-coverage (every excess strain value is above zero) over the range of injection amplitudes. Figure 20 shows the same excess plotted vs the injected spin-down value, where the search assumes a spin-down value of zero, and where
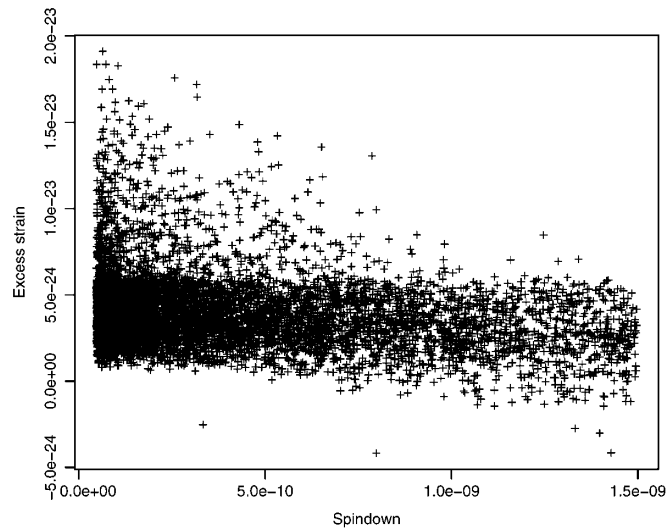

FIG. 20. Excess (upper limit minus injected) strain plotted vs injected signal spin-down for sample PowerFlux H1 elliptic polarization near 140 Hz injections.
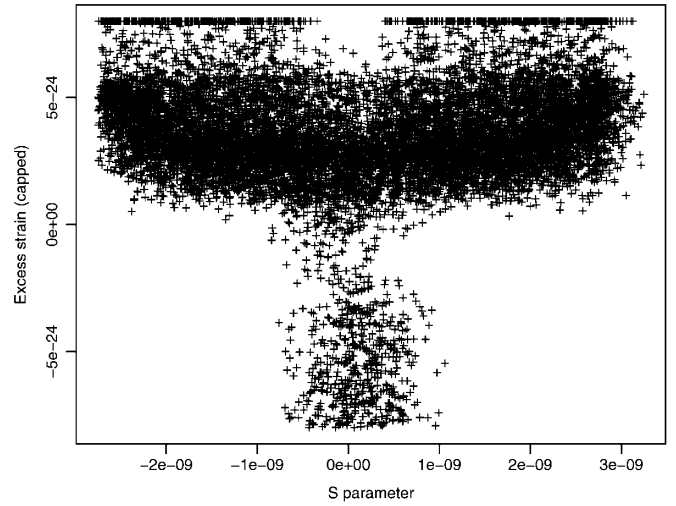

FIG. 21. Excess (upper limit minus injected) strain plotted vs S parameter defined in text, where values greater than 8×10^{-24} have been "capped" at that ceiling value.

the sample includes injections with actual spin-down values more than a step size away from the assumed value for the search template. As one can see, in this frequency range, a spin-down step size of 1.0×10^{-9} Hz s^{-1} is safe (true spin-down no more than 5.0×10^{-10} Hz s^{-1} away from the assumed search value). Figure 21 shows the excess plotted vs the S parameter that discriminates between sky regions of low and high Doppler stationarity. As shown, a value of $S_{large} \sim 1 \times 10^{-9}$ Hz s^{-1} is safe for these injections. For this search we have chosen 51 spin-down steps of 2×10^{-10} Hz s^{-1} for 50–225 Hz and 11 steps of 1×10^{-9} Hz s^{-1} for 200–1000 Hz.

More computationally intensive full time-domain signal injections were also carried out and the results found to be consistent with those from power injections, within statistical errors.

In addition, the PowerFlux method was validated with the hardware signal injections summarized in Table V. The PowerFlux algorithm was run on all 10 isolated pulsars, including two outside the 50–1000 Hz search region, and results found to agree well with expectation for the strengths of the signals and the noise levels in their bands. Table VIII shows the results of the analysis for the six pulsars for which a detection with SNR > 7 is obtained by PowerFlux for one or both of the 4 km interferometers. Figure 22 shows a sky map of PowerFlux $\psi = 0$ polarization SNR for the 0.25 Hz band containing pulsar 2 (575.16 Hz).

VII. RESULTS

All three methods described in Secs. IV and V have been applied in an all-sky search over a frequency range 50–1000 Hz. As described below, no evidence for a gravitational-wave signal is observed in any of the searches, and upper limits on sources are determined. For

TABLE VIII.   Results of PowerFlux analysis of the six S4 hardware pulsar injections for which there is detection ($SNR > 7$). Shown are the true nominal pulsar frequency at the start of the run (SSB frame), the frequency in each interferometer for detected signals, the true h_0 value of the injection, the worst-case upper limit from each interferometer, the polarization state for which the SNR is maximum in each interferometer, and the SNR of detected candidates.

| Pulsar | f_0 (Hz) | Detected f_0 (Hz) | | True h_0 | h_0 upper limit | | Detected polarization | | Detected SNR | |
		H1	L1		H1	L1	H1	L1	H1	L1
Pulsar2	575.164	575.161	575.164	8.04×10^{-24}	3.18×10^{-23}	2.16×10^{-23}	circular	circular	16.59	15.33
Pulsar3	108.857	108.858	108.858	3.26×10^{-23}	3.92×10^{-23}	3.36×10^{-23}	circular	linear	328.59	209.99
Pulsar4	1402.110	1402.111	1402.113	4.56×10^{-22}	6.50×10^{-22}	5.32×10^{-22}	linear	circular	2765.71	1651.82
Pulsar7	1220.933	1220.933	—	1.32×10^{-23}	3.56×10^{-23}	2.88×10^{-23}	circular	—	8.89	—
Pulsar8	193.950	193.951	193.948	3.18×10^{-23}	4.18×10^{-23}	3.52×10^{-23}	linear	circular	289.11	292.13
Pulsar9	763.847	763.849	—	8.13×10^{-24}	1.69×10^{-23}	1.97×10^{-23}	circular	—	8.18	—
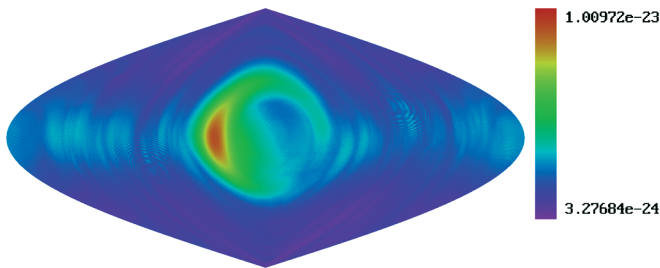
FIG. 22 (color).   Sample sky map of Feldman-Cousins upper limits on circularly polarized strain for a 0.25 Hz band containing hardware-injected Pulsar2 at 575.16 Hz. Only the data (half the run) during which the pulsar injection was enabled has been analyzed for this plot. The injected pulsar ($h_0 = 8.0 \times 10^{-24}$) stands out clearly above background. (Right ascension increases positively toward the left and declination toward the top of the sky map.)

the StackSlide and Hough methods, 95% confidence-level frequentist upper limits are placed on putative rotating neutron stars, assuming a uniform-sky and isotropic-orientation parent sample. Depending on the source location and inclination, these limits may over-cover or under-cover the true 95% confidence-level band. For the PowerFlux method, strict frequentist upper limits are placed on linearly and circularly polarized periodic gravitational-wave sources, assuming *worst-case* sky location, avoiding under-coverage. The limits on linear polarization are also reinterpreted as limits on rotating neutron stars, assuming worst-case sky location and worst-case star inclination. The following subsections describe these results in detail.

A. StackSlide results

1. Loudest powers and coincidence outliers

The StackSlide method was applied to the S4 H1 and L1 data set, as given in Sec. V B. As described in that section, only the loudest StackSlide Power was returned from a

search of the entire sky, the range of the frequency's time derivative, $[-1 \times 10^{-8}, 0]$ Hz s^{-1}, and for each 0.25 Hz band within 50–1000 Hz. The results are shown in Fig. 23.

Many of the StackSlide results have power greater than expected due to random chance alone (for Gaussian noise). To identify the most interesting subset of these cases, a simple coincidence test was applied: only results with an SNR greater than 7 in both H1 and L1 and with a fractional difference in frequency, measured in the SSB, less than or equal to 2.2×10^{-4} were identified as outliers for further follow up. The requirement on frequency agreement comes from the worst-case scenario where a signal is detected on opposite sides of the sky with opposite Doppler shifts of $1 + v/c$ and $1 - v/c$, giving a maximum fraction difference in the detected frequency at the SSB of $2v/c \leq 2.2 \times 10^{-4}$. The results after applying this simple coincidence test are shown in Fig. 24. The outliers that passed the test are shown in Table IX.

Note that the coincidence test used on the StackSlide results is very conservative in that it only covers the worst-
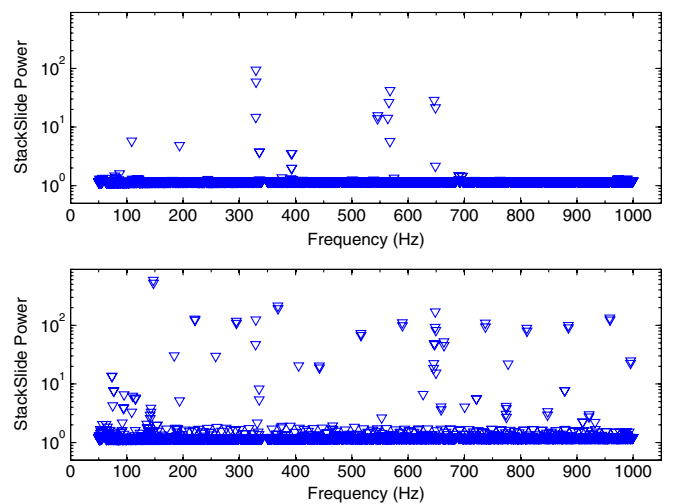

FIG. 23 (color online).   The loudest observed StackSlide Power for H1 (top) and L1 (bottom). Frequency bands with the harmonics of 60 Hz and the violin modes have been removed.
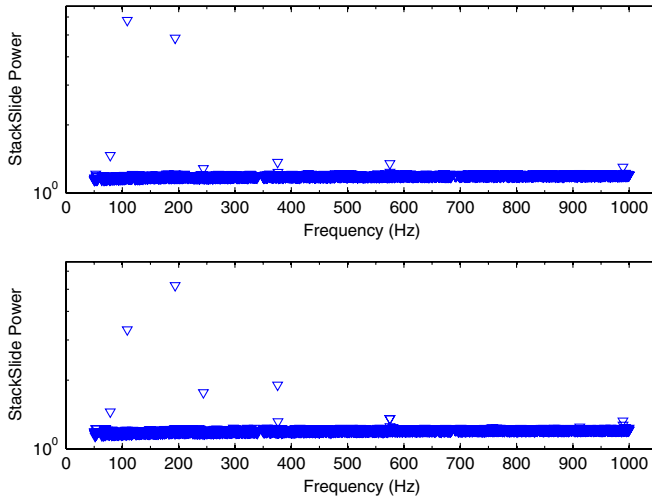
FIG. 24 (color online). The loudest observed StackSlide Power for H1 (top) and L1 (bottom) with a simple veto applied: only outliers in each 0.25 Hz band with SNR > 7 in both interferometers that have a fractional frequency difference $\leq 2.2 \times 10^{-4}$ are kept. These are shown against the background results that have SNR ≤ 7 in both interferometers. Frequency bands with the harmonics of 60 Hz and the violin modes have also been removed.

case frequency difference, and makes no requirement on consistency in sky position or the frequency's time derivative. However it is meant to find only the most prominent outliers. Since an automated follow up of possible candidates is not yet in place, the follow up is carried out manually. This dictated using a large threshold on SNR. Also, since the false-dismissal rate of the coincidence test used was not determined (though it is assumed to be essentially zero) it is not used in this paper when setting upper limits. Monte Carlo studies will be needed to find

appropriate thresholds on SNR and the size of coincidence windows, so that proper false-alarm and false-dismissal rates can be determined; such studies will be carried out when analyzing future data sets.

Three types of qualitative follow-up tests were performed on each of the outliers in Table IX. First, using the sky position and the $\dot{f}$ value of the template that gives the outlier in H1, the StackSlide Power was found using the same values for these in L1 and H2 for a frequency band around that of the outlier in H1. For a fixed sky position and $\dot{f}$, a true gravitational-wave signal should show up in all three detectors as a narrow line at nearly the same frequency (though with a SNR corresponding to half the length displacement in H2 compared with that in H1 and L1). Second, the StackSlide Power was computed for the frequency bands containing the outliers, with sliding turned off. If an instrumental line is the underlying cause of the outlier, a stronger and narrower peak will tend to show up in this case. Third, the StackSlide Power was computed for each H1 outlier template, using half (and some other fractions) of the data. This should reduce the SNR of a true signal by roughly the square root of the fractional reduction of the data, but identify transient signals, which would fail this test by showing up in certain stretches of the data with more SNR while disappearing in other stretches. This would be true of the hardware injections which were not always on during the run, or temporary disturbances of the instrument which appear to look like signals only for limited periods of time. (The search described here was not designed to find truly transient gravitational-wave signals.)

The follow-up tests on the outliers given in Table IX found that none is qualitatively consistent with a true gravitational-wave signal. The three loudest hardware injections of periodic gravitational waves from fake isolated

TABLE IX. StackSlide outliers with SNR > 7 in both interferometers, with fraction difference in frequency less than or equal to 2.2×10^{-4}, and after removal of the bands with 60 Hz harmonics and the violin modes.

|	f_{H1} (Hz)	f_{L1} (Hz)	H1 SNR	L1 SNR	Comment
1	78.618 889	78.618 889	14.82	13.58	Inst. Lines
2	108.856 111	108.856 111	152.11	69.79	HW Inj. Pulsar3
3	193.947 778	193.949 444	121.89	125.75	HW Inj. Pulsar8
4	244.148 889	244.157 778	9.00	22.89	Inst. Lines
5	375.793 889	375.806 667	11.68	27.09	HW Inj. Pulsar11
6	376.271 111	376.281 667	7.47	9.46	HW Inj. Pulsar11
7	575.162 778	575.153 333	11.09	10.71	HW Inj. Pulsar2
8	575.250 000	575.371 667	7.49	7.51	Inst. Lines
9	575.250 000	575.153 333	7.49	10.71	Inst. and Pulsar2
10	580.682 778	580.734 444	7.02	7.19	Inst. Lines
11	912.307 778	912.271 111	7.02	7.37	Inst. Lines
12	988.919 444	988.960 556	9.56	9.75	Inst. Lines
13	988.919 444	989.000 000	9.56	8.12	Inst. Lines
14	993.356 111	993.523 333	7.08	7.12	Inst. Lines
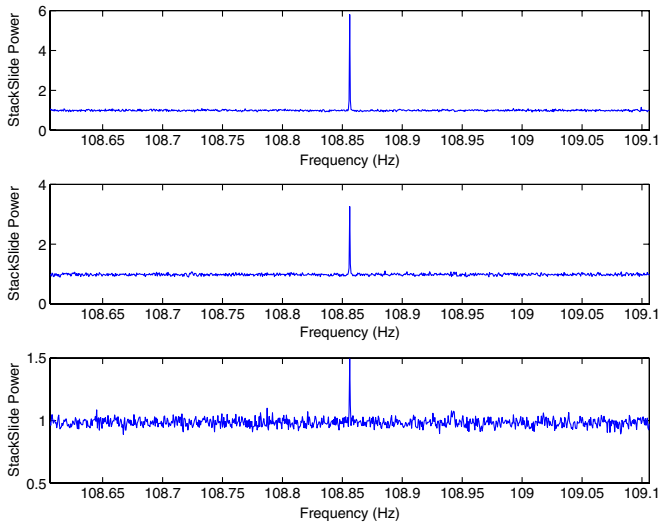
FIG. 25 (color online). The StackSlide Power vs frequency for H1 (top), L1 (middle), and H2 (bottom) using the sky position and the $\dot{f}$ value of the template that gives the outlier in H1, for outlier number 2 given in Table IX. Comparing with Tables V and VI this outlier is identified as due to hardware injection Pulsar3.

sources were found (indicated as Pulsar3, Pulsar8, and Pulsar2), as well as interference from a fake source in a binary system (Pulsar11). All of the outliers due to the hardware injections show up in the H1 template as relatively narrow lines in all three detectors, for example, as shown in Fig. 25. These outliers, on the other hand, fail the third test when looking at times the hardware injections were turned off. In particular, this test, along with the frequencies in Table V, confirms the identification of outliers 5 and 6 as due to Pulsar11. The other hardware injections also are identified as such via their detected frequencies in Table V and SNRs in Table VI. In comparison, none of the other outliers qualitatively passes the first test, for example, as shown in Fig. 26. The second test was less conclusive, since some of the outliers lie at points on the sky that receive little Doppler modulation, but based on the first test we conclude that the remaining outliers are only consistent with instrumental line artifacts. These results are summarized in column six of Table IX. In future searches, tests of the type used here should be studied using Monte Carlo simulations, to make them more quantitative.

2. StackSlide upper limits

The StackSlide 95% confidence upper limits on h_0 are shown as crosses for H1 (top) and L1 (bottom), respectively, in Fig. 27, while the solid curves in this figure show the corresponding characteristic amplitudes given by Eq. (B11) in Appendix B. The characteristic amplitudes were calculated using an estimate of the noise from a typical time during the run, but include bands with the power line and violin line harmonics which were excluded
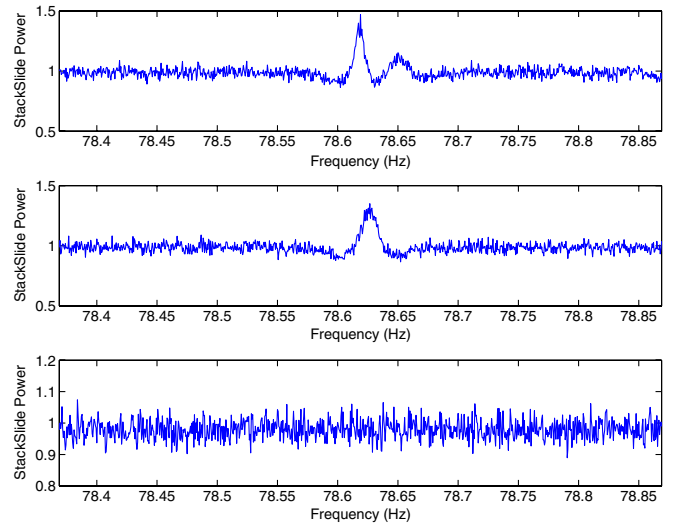

FIG. 26 (color online). The StackSlide Power vs frequency for H1 (top), L1 (middle), and H2 (bottom) using the sky position and the $\dot{f}$ value of the template that gives the outlier in H1 for outlier number 1 given in Table IX.

from the StackSlide search. The best upper limits over the entire search band are given in Table X. The uncertainties in the upper limits and confidence due to the method used are less than or equal to 3% and 5.3%, respectively; random and systematic errors from the calibration increase these uncertainties to about 10%.

B. Hough results

1. Number counts

For the S4 data set, there are a total of $N = 2966$ SFTs from the three interferometers, giving an expected average
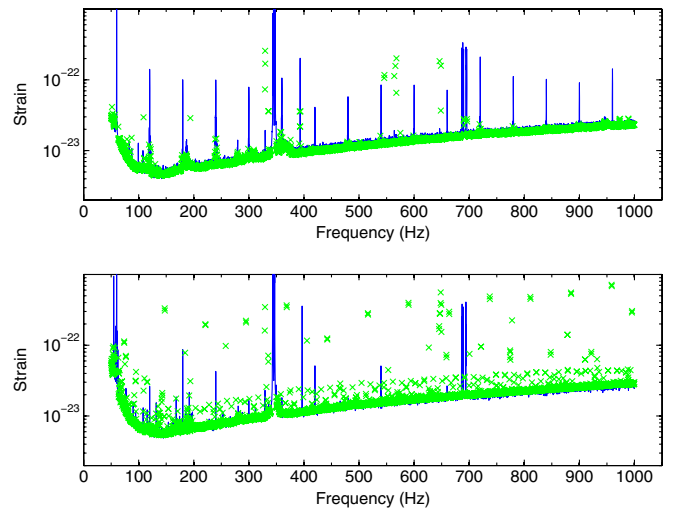

FIG. 27 (color online). The solid curve shows the characteristic amplitude given by Eq. (B11) and crosses show the measured upper limits on h_0 for the StackSlide search of the H1 (top) and L1 (bottom) data.

TABLE X.   Best StackSlide all-sky h_0 upper limits obtained on the strength of gravitational waves from isolated neutron stars.

Detector	Band (Hz)	$h_0^{95\%}$
H1	139.50–139.75	4.39×10^{-24}
L1	140.75–141.00	5.36×10^{-24}

number count for pure noise of $\bar{n} = Np \sim 593$. The standard deviation σ now depends on the sky-patch according to (27). For reference, if we had chosen unit weights, the standard deviation assuming pure Gaussian noise would have been ~ 22 for the multi-interferometer search. To compare number counts directly across different sky patches, we employ the *significance s* of a number count defined in Eq. (29).

Since the three interferometers have different noise floors and duty factors, we would like to know their relative contributions to the total Hough number count, and whether any of the interferometers should be excluded from the search, or if all of them should be included. For this purpose, for the moment let us ignore the beam-pattern functions and consider just the noise weighting: $w_i \propto 1/S_i$. The relative contribution of a particular interferometer, say I, is given by the ratio

$$r_I = \frac{\sum_{i \in I} w_i}{\sum_{i=1}^N w_i}, \qquad I = \text{H1, L1, H2.} \qquad (40)$$

The numerator is a sum of the weights for the Ith interferometer while the denominator is the sum of all the weights. This figure-of-merit incorporates both the noise level of data from an interferometer, and also its duty cycle as determined by the number of SFTs available for that interferometer. Figure 28 shows the relative contributions from H1, L1, and H2 for the duration of the S4 run. From
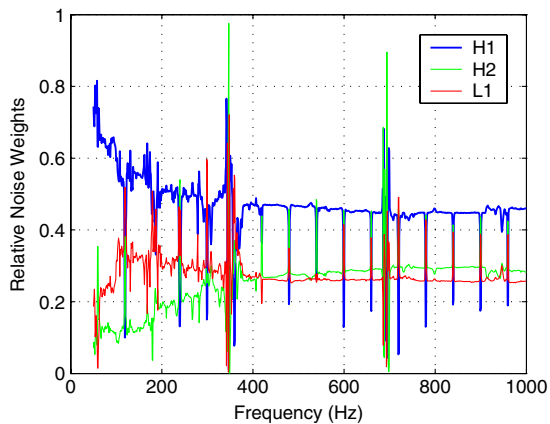

FIG. 28 (color online).   Relative contributions of the three interferometers in the Hough multi-interferometer search. The noise weights are calculated in 1 Hz bands.
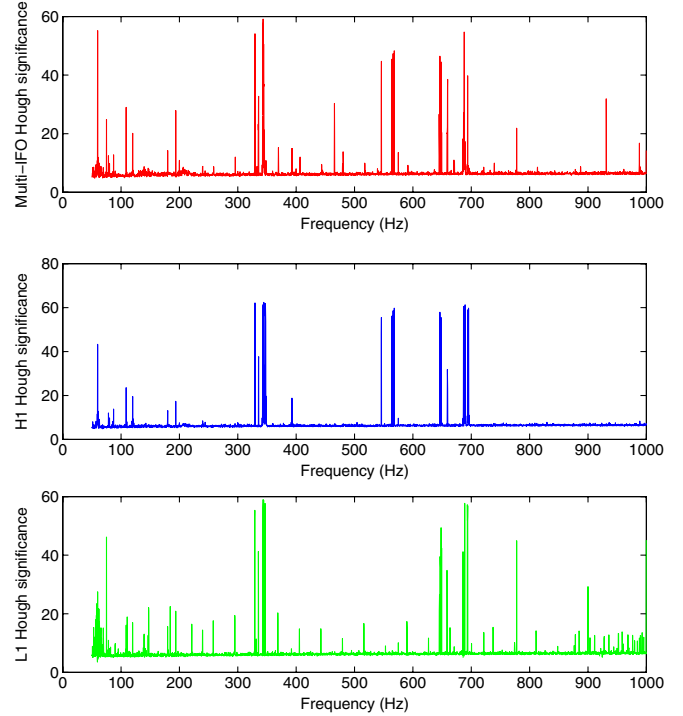

FIG. 29 (color online).   The measured loudest significance in each 0.25 Hz from the Hough search of the multi-interferometer (top), H1 (middle), and L1(bottom) data.

the plot, we see that H1 clearly contributes the most. H2 contributes least at low frequencies while L1 contributes least at higher frequencies. Hence all three LIGO interferometers are included in this search. For comparison purposes and for coincidence analysis, we have also analyzed the data from H1 and L1 separately.

Figure 29 shows the result of the Hough search using data from all three LIGO interferometers, either combined in a multi-interferometer search, or just for H1 and L1 data. This figure shows the loudest significance in every 0.25 Hz band, maximized over all sky positions, frequencies, and spin-downs for the three searches. Line cleaning was used as described before. In the bands in which there are no spectral disturbances the significance distribution agrees very well with the theoretical expected distribution as was shown in Fig. 8.

2. Study of coincidence outliers

There are many outliers from the Hough search with significance values higher than expected for Gaussian noise, as shown in Fig. 29. Many of the large outliers correspond to well-known instrumental artifacts described earlier, such as the power mains harmonics or the violin modes.

Note the relation between significance and false alarm which can be derived from Eqs. (28) and (29) for Gaussian noise:

$$\alpha_H = 0.5\mathrm{erfc}(s/\sqrt{2}). \tag{41}$$

To identify interesting candidates, we consider only those that have a significance greater than 7 in the multi-interferometer search (the most sensitive one). This is the same threshold considered by the StackSlide and PowerFlux searches. For the Hough search, this threshold corresponds to a false-alarm rate of 1.3×10^{-12}. With this threshold, we would expect about 6 candidates in a 100 Hz band around 1 kHz for Gaussian noise, since the number of templates analyzed in a 1 Hz band around 1 kHz is about $n = 4.4 \times 10^{10}$. If we would like to set a different threshold in order to select, say one event in a 1 Hz band, then we should increase the false alarm to $\alpha_H = 1/n = 2.2 \times 10^{-11}$.

In order to exclude spurious events due to instrumental noise in just one detector, we pass these candidates through a simple coincidence test in both the H1 and the L1 data. Since the single detector search is less sensitive than the multi-interferometer one, we consider events from H1 and L1 with a significance greater than 6.6, corresponding to a false-alarm rate of 2.0×10^{-11}. The numbers of templates analyzed using the H1 or L1 data are the same as for the multi-interferometer search.

The coincidence test applied first in frequency is similar to the one described for the StackSlide search, using a coincidence frequency window as broad as the size of the maximum Doppler shift expected at a given frequency. Of the initial 3800 0.25 Hz bands investigated, 276 yielded outliers in the multi-interferometer search with a significance higher than 7. Requiring those bands (or neighboring bands) to have outliers in H1 higher than 6.6, reduced by half the number of surviving bands. These remaining bands were studied in detail and, after eliminating power line harmonics and the violin modes, 27 candidates remained. Applying again the same coincidence test with the L1 data, we are left with only 7 coincidence outliers that are listed on Table XI and displayed in Fig. 30.

Except for the third outlier, the coincidence can be attributed to instrumental lines in the detectors or to the hardware pulsar injections. Table XII summarizes the pa-
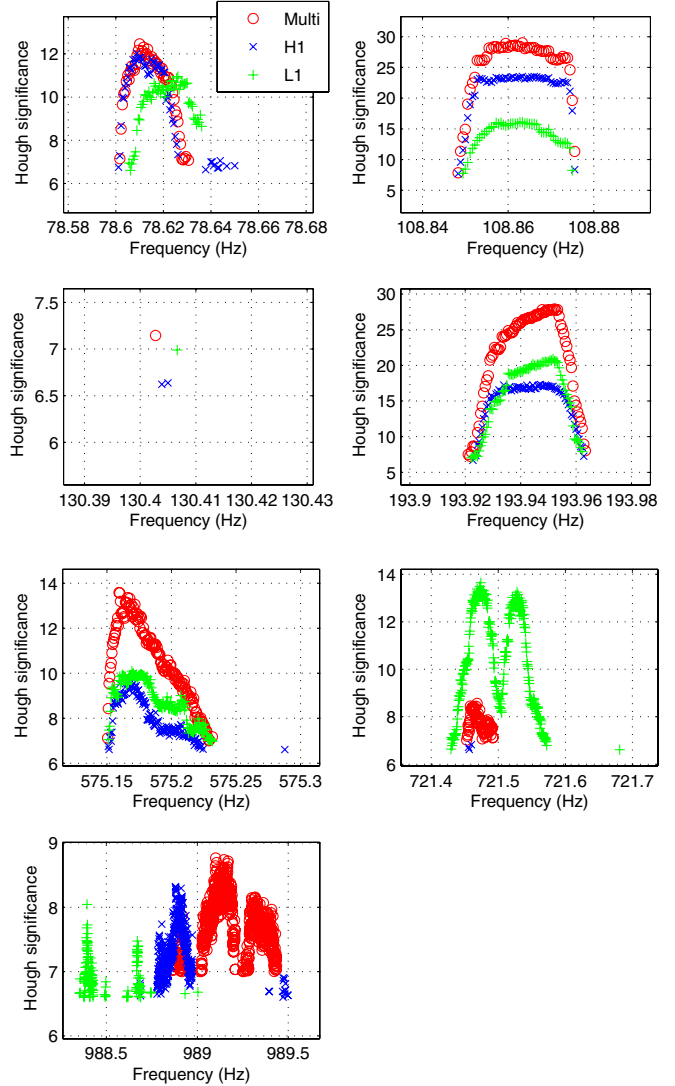

FIG. 30 (color online). Hough significance of the outliers that have survived the coincidence analysis without considering the bands contaminated with 60 Hz harmonics or the violin modes. Points are plotted only for multi-interferometer templates with significance greater than 7 and for single-interferometer templates with significance greater than 6.6.

rameters of the third coincidence candidate in the 130.40–130.41 Hz frequency band, including all the events that in any of the searches had a significance larger than 6.6. As can be seen from the table, the events from the different data sets correspond to widely separated sky locations. Hence no detections were made in the Hough search of the S4 data.

In future searches we plan to use lower thresholds in the semicoherent step in order to point to interesting areas in parameter space to be followed up, using a hierarchical scheme with alternating coherent and semicoherent steps. In what follows we will concentrate on setting upper limits on the amplitude h_0 in each of the 0.25 Hz bands.

TABLE XI. Hough outliers that have survived the coincidence analysis in frequency, excluding those related to 60 Hz harmonics and the violin modes.

		Hough significance			
	Band (Hz)	Multi-IFO	H1	L1	Comment
1	78.602–78.631	12.466	12.023	10.953	Inst. Lines
2	108.850–108.875	29.006	23.528	16.090	Inj. Pulsar3
3	130.402–130.407	7.146	6.637	6.989	?
4	193.92–193.96	27.911	17.327	20.890	Inj. Pulsar8
5	575.15–575.23	13.584	9.620	10.097	Inj. Pulsar2
6	721.45–721.50	8.560	6.821	13.647	L1 Inst. Lines
7	988.80–988.95	7.873	8.322	7.475	Inst. Lines

TABLE XII. Parameters of the candidate events with a significance greater than 6.6 in the multi-interferometer, H1, and L1 data searches around the Hough outlier number 3. The parameters correspond to the significance, frequency, and spin-down for the reference time of the beginning of S4, and sky locations.

Detector	s	f_0 (Hz)	df/dt (Hz s^{-1})	α (rad)	δ (rad)
Multi-IFO	7.146	130.4028	-1.745×10^{-9}	0.8798	-1.2385
H1	6.622	130.4039	-1.334×10^{-9}	2.1889	0.7797
H1	6.637	130.4050	-1.334×10^{-9}	2.0556	0.6115
L1	6.989	130.4067	-1.963×10^{-9}	1.1690	-1.0104

3. Upper limits

As in the previous S2 Hough search [7], we set a population-based frequentist upper limit using Monte Carlo signal software injections. We draw attention to two important differences from that analysis:

(i) In [7], known spectral disturbances were handled by simply avoiding all the frequency bins which could have been affected by Doppler broadening. Thus, the loudest event was obtained by excluding such frequency bins, and the subsequent Monte Carlo simulations also did not perform any signal injections in these bins. Here we follow the same approach as used in the StackSlide search; we use the spectral line removal procedure described in Sec. V B 1. For consistency, the same line removal procedure is followed in the Monte Carlo simulation after every software injection.

(ii) Recall that the calculation of the weights depends on the sky patch, and the search has been carried out by breaking up the sky in 92 patches. Thus, for every randomly injected signal, we calculate the weights corresponding to the center of the corresponding sky patch. The analysis of [7] did not use any weights and this extra step was not required.

The 95% confidence all-sky upper-limit results on h_0 from the Hough search for the multi-interferometer, H1 and L1 data are shown in Fig. 31. These upper limits have been obtained by means of Monte Carlo injections in each 0.25 Hz band in the same way as described in [7]. The best upper limit over the entire search band corresponds to 4.28×10^{-24} for the multi-interferometer case in the 140.00–140.25 Hz band. The results are summarized in Table XIII.

Let us now understand some features of the upper-limit results. First, it turns out that it is possible to accurately estimate the upper limits without extensive Monte Carlo simulations. From (30), and setting $w_i \propto X_i$, we expect that the upper limits are

$$h_0^{95\%} \propto \left(\frac{1}{||\mathbf{X}||}\right)^{1/2} \sqrt{\frac{\mathcal{S}}{T_{\mathrm{coh}}}}. \tag{42}$$

Recall that X_i contains contributions both from the sky location-dependent antenna pattern functions and from the sky location-independent noise floor estimates. However, since we are setting upper limits for a population uniformly distributed in the sky, we might expect that the S_i are more important for estimating the value of $h_0^{95\%}$. From Eq. (32) and averaging over the sky we get

$$||\mathbf{X}|| \propto \sqrt{\sum_{i=0}^{N-1}\left(\frac{1}{S_i}\right)^2}, \tag{43}$$

and thus, up to a constant factor C, the estimated upper limits are given by

$$h_0^{95\%} = C\left(\frac{1}{\sum_{i=0}^{N-1}(S_i)^{-2}}\right)^{1/4} \sqrt{\frac{\mathcal{S}}{T_{\mathrm{coh}}}}. \tag{44}$$

The value of $\mathcal{S}$ is calculated from Eq. (31) using the false alarm α_{H} corresponding to the significance of the observed loudest event in a particular frequency band. The value of
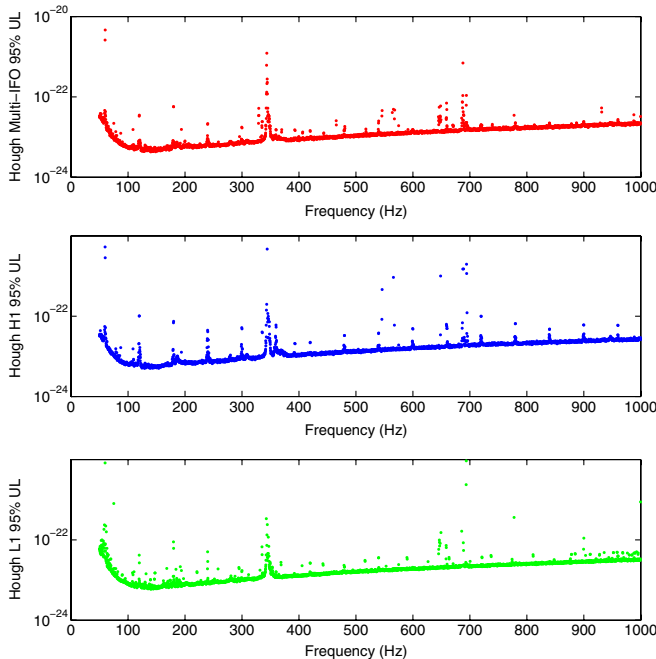

FIG. 31 (color online). The 95% confidence all-sky upper limits on h_0 from the Hough search of the multi-interferometer (top), H1 (middle), and L1 (bottom) data. These upper limits have been obtained by means of Monte Carlo injections in each 0.25 Hz band.

TABLE XIII. Best Hough all-sky upper limits obtained on the strength of gravitational waves from isolated neutron stars.

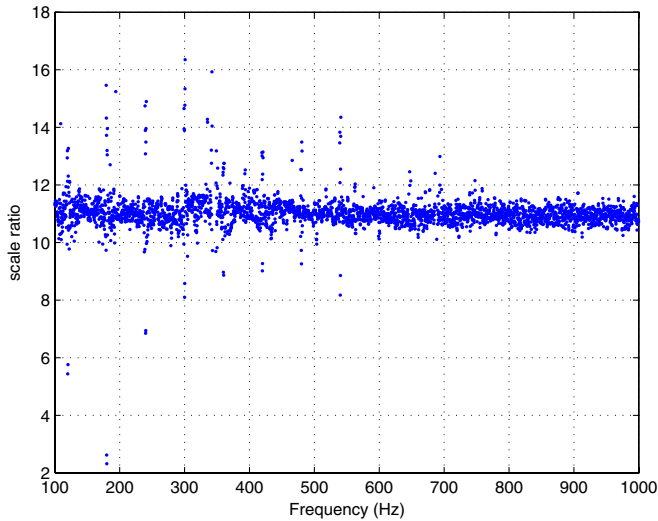| Detector	Band (Hz)	$h_0^{95\%}$
H1 + H2 + L1	140.00–140.25	4.28×10^{-24}
H1	129.00–129.25	5.02×10^{-24}
L1	140.25–140.50	5.89×10^{-24}

FIG. 32 (color online). Ratio of the upper limits measured by means of Monte Carlo injections in the multi-interferometer Hough search to the quantity $h_0^{95\%}/C$ as defined in Eq. (44). The value of $\mathcal{S}$ in Eq. (44) is computed using the false alarm α_H corresponding to the observed loudest event, in a given frequency band, and for a false-dismissal rate $\beta_H = 0.05$, in correspondence to the desired confidence level of the upper limit. The comparison is performed in each 0.25 Hz band. Analysis of the full bandwidth, and also in different 100 Hz bands, yield a scale factor C to be 11.0 ± 0.5.

the false-dismissal rate β_H corresponds to the desired confidence level of the upper limit (in this case 95%). To show that such a fit is viable, Fig. 32 plots the value of the constant C appearing in the above equation for every
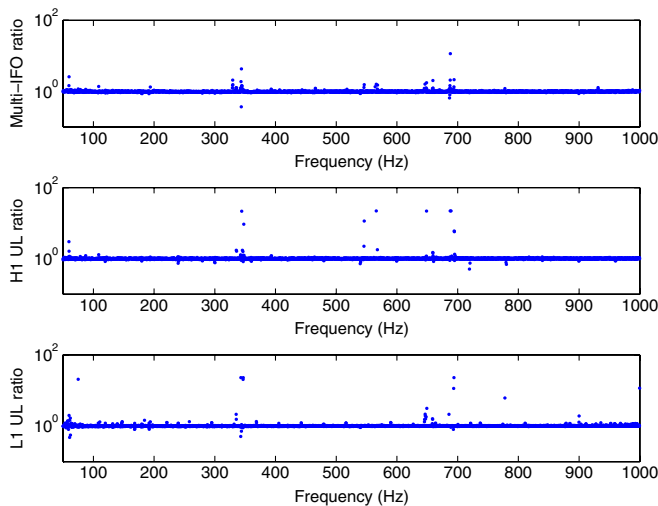

FIG. 33 (color online). Ratio of the 95% confidence all-sky upper limits on h_0 obtained from the Hough search by means of Monte Carlo injections to those predicted by Eq. (44) of the multi-interferometer (top), H1 (middle), and L1 (bottom) data. The comparison is performed in 0.25 Hz bands. The scale factors C used are 11.0 for the multi-interferometer search, 11.5 for H1, and 11.1 for L1.

0.25 Hz frequency band, using the measured upper limits. It turns out that $C = 11.0 \pm 0.5$. The exact value of C depends on the interferometer and the search performed, but it is still found to lie within this range. This scale factor $C = 11.0 \pm 0.5$ is about 2 times worse than we would expect if we were performing a targeted (multi-interferometer with weights) search with no mismatch. This factor of 2 is also in very good agreement with what was reported in the S2 search [7].

The utility of this fit is that having determined the value of C in a small frequency range, it can be extrapolated to cover the full bandwidth without performing any further Monte Carlo simulations. Figure 33 plots the ratio of the measured upper limits to the estimated values showing the accuracy of the fit. The scale factors C used are 11.0 for the multi-interferometer search, 11.5 for H1, and 11.1 for L1. The scale factors have been obtained in all cases by comparing the measured upper limits by means of Monte Carlo injections to the quantity $h_0^{95\%}/C$ as defined in Eq. (44), using the full bandwidth of the search. These estimated upper limits have an error smaller than 5% for bands free of large instrumental disturbances.

We conclude this section by quantifying the improvement in sensitivity caused by using the weights. Figure 34 shows the comparison between the weighted and unweighted results in the 800–900 Hz frequency range. The average improvement is ~9% in this band. It is easy to see that the improvement as compared to the unweighted Hough search will be larger if the variation of S_i and the beam-pattern functions is large across the SFTs. Since the variation in S_i is larger in a multi-interferometer search, we expect this improvement to be much more significant in a
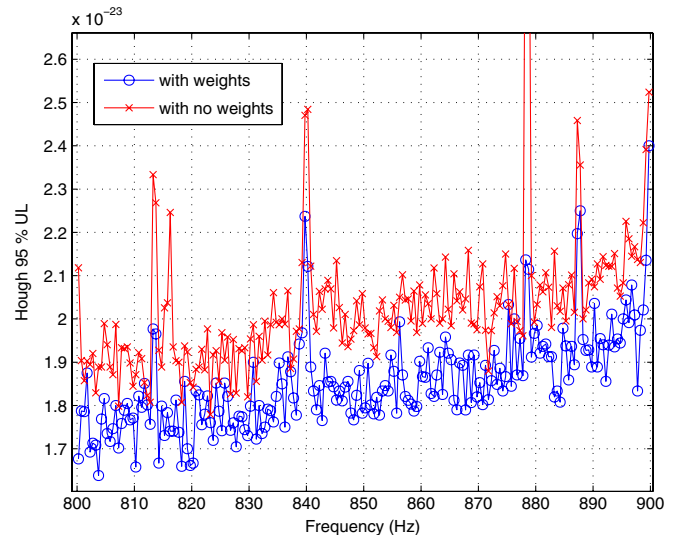

FIG. 34 (color online). Comparison of the upper limits obtained using 500 Monte Carlo injections with and without weights in 0.5 Hz bands for the Hough multi-interferometer search. The use of the weights improves the upper limits by a ~9% factor.

multi-interferometer search. For the case of analyzing data from a single interferometer, for example, H1, the improvement in the upper limits due to the weights turns out to be only ~6%. Also, the improvement can be increased by choosing smaller sky patches so that the weight calculation is more optimal. In particular, if there would not be any sky mismatch in computing the weights, only due to the amplitude modulation, i.e., in the presence of Gaussian and stationary noise, we would expect an average increase of sensitivity of ~10%, and it could be up to ~12% for optimally oriented pulsars. These results have been verified experimentally by means of a set of Monte Carlo tests [33].

C. PowerFlux results

1. Single-interferometer results

The PowerFlux method has been applied to the S4 data sample in the range 50–1000 Hz. Five polarization projections are sampled for each grid point: four linear polarizations with $\psi = 0$, $\pi/8$, $\pi/4$, $3\pi/8$; and circular polarization. For each sky grid point in the "good sky" defined above and each of the 501 frequency bins (there is a slight overlap of 0.25 Hz bands), the Feldman-Cousins [34] 95% CL upper limit is computed, as described in Sec. V D 5, for each polarization projection. Worst-case upper limits on linear polarization for each grid point and frequency are taken to be the highest linear-polarization-projection strain limit divided by $\cos(\pi/8)$ to correct for worst-case polarization mismatch. The highest limit for all frequency bins in the 0.25 Hz band and over all sampled sky points is taken to be the broad-sky limit for that 0.25 Hz
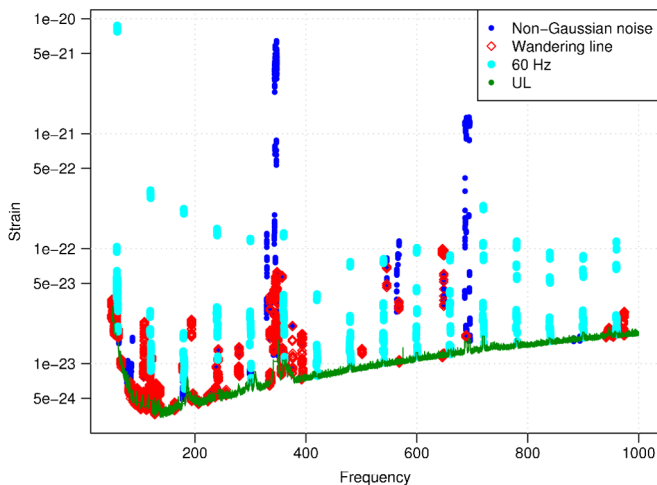

FIG. 35 (color online). PowerFlux limits on linearly polarized CW radiation amplitude for the H1 data from the S4 run. Bands flagged as non-Gaussian (instrumental artifacts) or near 60 Hz harmonics, and for which derived upper limits are unreliable, are indicated by color. Diamonds indicate bands for which wandering instrumental lines (or very strong injected signals) lead to degraded upper limits.
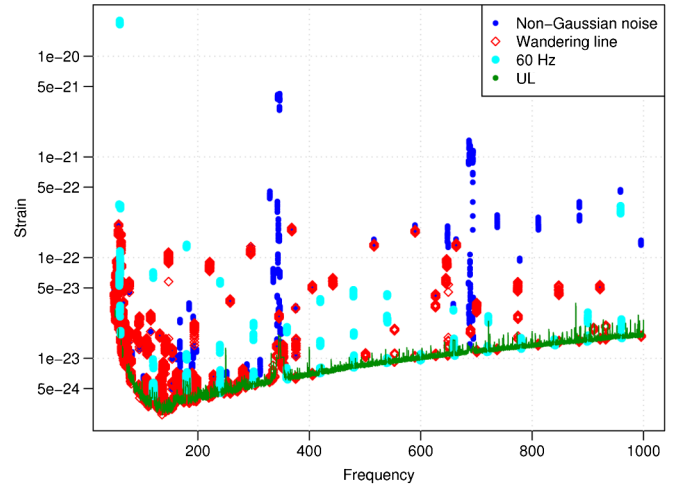

FIG. 36 (color online). PowerFlux limits on linearly polarized CW radiation amplitude for the L1 data from the S4 run, with the same color coding as in the preceding figure.

band. Figures 35 and 36 show the resulting broad-sky limits on linearly polarized periodic sources from H1 and L1. Bands flagged as non-Gaussian (instrumental artifacts leading to failure of the KS test) or near 60 Hz harmonics are indicated by color. The derived upper limits for these bands are considered unreliable. Diamonds indicate bands for which wandering instrumental lines (or very strong injected signals) lead to degraded upper limits. An exceedingly strong pulsar can be identified as a wandering line, and several strong hardware-injected pulsars are marked in the figures as such.

These limits on linearly polarized radiation and the corresponding limits on circularly polarized radiation can be interpreted as worst-case and best-case limits on a triaxial-ellipsoid, nonprecessing neutron star, respectively, as discussed in Appendix A. Multiplying the linear-polarization limits by a factor of 2 leads to the *worst-case* H1 limits on h_0 shown in Figs. 37 and 38. The circular-polarization limits require no scale correction. Note that the StackSlide and Hough H1 limits shown on the same figure apply to a uniform-sky, uniform-orientation population of pulsars.

2. Coincidence follow up of loud candidates

All outliers (SNR > 7, diamonds, and non-Gaussian bands) in the single-interferometer analysis are checked for coincidence between H1 and L1. In this follow up, agreement is required in frequency to within 10 mHz, in spin-down to within 1×10^{-10} Hz s^{-1}, and in both right ascension and declination to within 0.5 radians. The only surviving candidates are associated with hardware-injected pulsars 2, 3, 4, and 8 (see Table VIII), 1 Hz harmonics, violin modes, and instrumental lines in both detectors near 78.6 Hz (also seen in the StackSlide and Hough searches).

The source of these lines remains unknown, but follow-up consistency checks described in Sec. VII A rule out an astrophysical explanation.

From this coincidence analysis, we see no evidence of a strong pulsar signal in the S4 data. It should be noted, however, that the SNR threshold of 7 is relatively high. A lower threshold and a more refined algorithm for location and frequency coincidence is under development for future searches.

VIII. COMPARISON OF THE THREE METHODS

Figures 37 and 38 show superimposed the final upper limits on h_0 from the StackSlide, Hough, and PowerFlux methods when applied to the S4 single-interferometer H1 and L1 data, respectively. As one might have expected, we see that the StackSlide and Hough population-based limits lie between the best-case and worst-case h_0 strict limits from PowerFlux. As indicated in Figs. 37 and 38, the
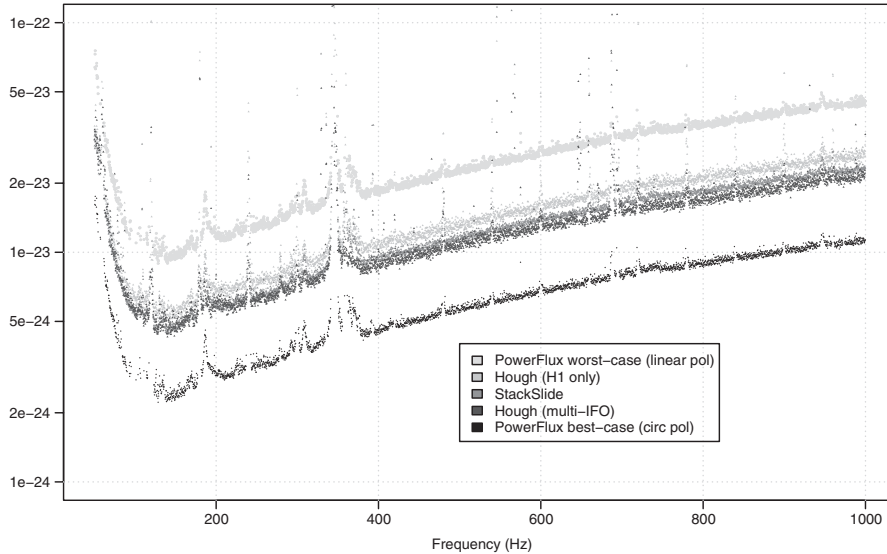

FIG. 37. H1 upper limits (95% CL) on h_0 from the three methods. The StackSlide and Hough limits are population based, while those from PowerFlux are strict and apply, respectively, to the most favorable and least favorable pulsar inclinations. Also shown are the multi-interferometer limits from the Hough search.
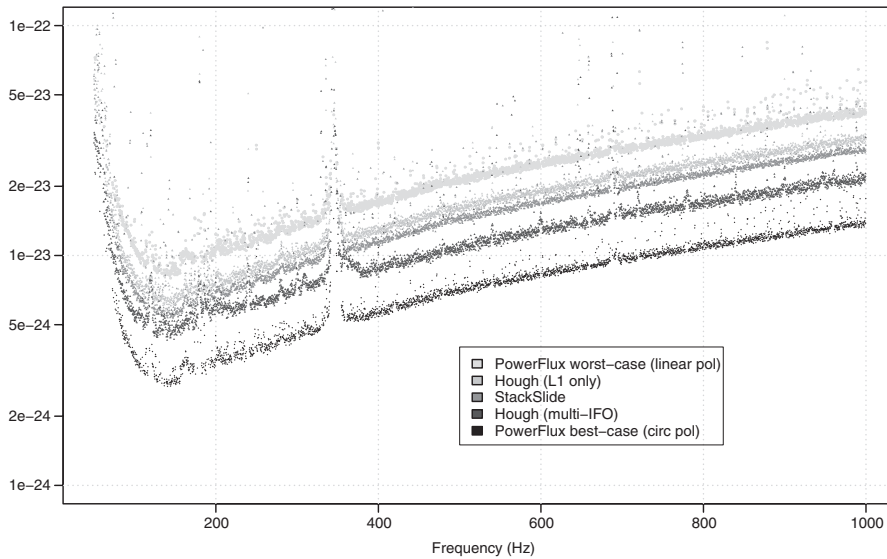

FIG. 38. L1 Upper limits (95% CL) on h_0 from the three methods. The StackSlide and Hough limits are population based, while those from PowerFlux are strict and apply, respectively, to the most favorable and least favorable pulsar inclinations. Also shown are the multi-interferometer limits from the Hough search.

Hough search sensitivity improves with the summing of powers from two or more interferometers.

To be more precise as to expectations, we have directly compared detection efficiencies of the three methods in frequency bands with different noise characteristics. As discussed above, we expect overall improved performance of Powerflux with respect to StackSlide and Hough, except possibly for frequency bands marked by extreme non-Gaussianity or nonstationarity, where the Hough integer truncation of extreme power outliers can provide more robustness. We do not consider computational efficiency, which could play an important role in deciding which algorithm to use in computationally limited hierarchical searches.

A comparison is shown in Figs. 39 and 40 among the efficiencies of the three methods for two particular 0.25 Hz bands for H1: 140.5–140.75 Hz and 357–357.25 Hz. The horizontal axis in each case is the h_0 of Monte Carlo software injections with random sky locations, spin-downs, and orientations. The noise in the two bands have qualitatively different features. The 140.5–140.75 Hz band is a typical "clean" band with Gaussian noise and no observable spectral features. As expected, Fig. 39 shows that the efficiency for the PowerFlux method is higher than that for StackSlide, while that of StackSlide is better than that for Hough. In other bands, where there are stationary spectral disturbances, we find that PowerFlux remains the most efficient method.

The noise in the band 357–357.25 Hz is non-Gaussian and displays a large transient spectral disturbance, in addition to stationary line noise at 357 Hz itself. The stationary 357 Hz line was removed during the StackSlide and Hough searches, avoided during the PowerFlux search, and handled self-consistently during Monte Carlo software injections. In this band, the Hough transform method
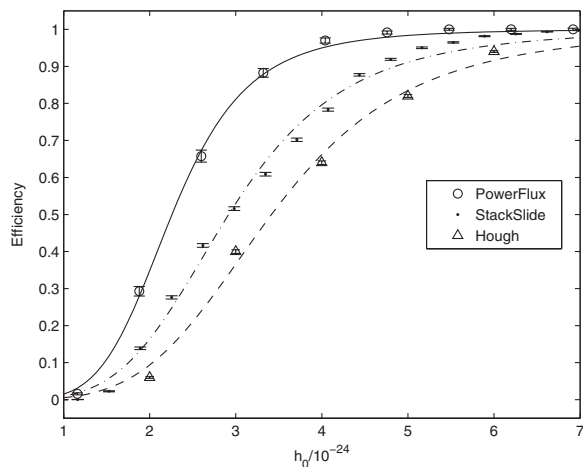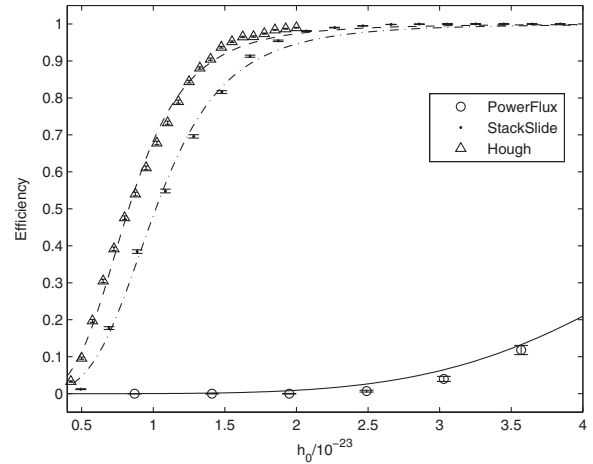

FIG. 40. Detection efficiency curves for the frequency band 357–357.25 Hz, for H1. This band has a transient spectral disturbance affecting some of the SFTs. The Hough transform method proves to be robust against such nonstationarities and is more sensitive than StackSlide or PowerFlux in this band. The SNR thresholds used to generate these curves were 6.3, 5.2, and 30, respectively, for the StackSlide, Hough, and PowerFlux methods, where the StackSlide and PowerFlux thresholds correspond to the loudest candidates in that band in the data.

proves to be robust against transient noise, and more sensitive than the StackSlide or PowerFlux implementations (see Fig. 39). In fact, no PowerFlux upper limit is quoted for this band because of the large non-Gaussianity detected during noise decomposition. Note that the SNR thresholds used for Stackslide, Hough, and PowerFlux in Fig. 40 are set to 6.3, 5.2, and 30, respectively, to match their loudest events in this band of the data.

IX. SUMMARY, ASTROPHYSICAL REACH, AND OUTLOOK

In summary, we have set upper limits on the strength of continuous-wave gravitational radiation over a range in frequencies from 50 Hz to 1000 Hz, using three different semicoherent methods for summing of strain power from the LIGO interferometers. Upper limits have been derived using both a population-based method applicable to the entire sky and a strict method applicable to regions of the sky for which received frequencies were not stationary during the S4 data run.

The limits have been interpreted in terms of amplitudes h_0 for pulsars and in terms of linear and circular polarization amplitudes, corresponding to least favorable and most favorable pulsar inclinations, respectively. As a reminder, sets of known instrumental spectral lines have been cleaned from the data prior to setting the population-based StackSlide and Hough upper limits (Tables II, III, and IV), while regions of the sky (defined by cutoff values on the S parameter (Eqs. (38) and (39)) have been excluded in the

FIG. 39. Comparison of StackSlide, Hough, and PowerFlux efficiencies (SNR > 7) vs injected strain amplitude h_0 for the band 140.50–140.75 Hz for H1. From left to right, the curves correspond to PowerFlux, StackSlide, and Hough. This band is typical of those without large outliers.

strict PowerFlux upper limits. The numerical values of the upper limits can be obtained separately [35].

We have reached an important milestone on the road to astrophysically interesting all-sky results: Our best upper limits on h_0 are comparable to the value of a few times 10^{-24} at which one might optimistically expect to see the strongest signal from a previously unknown neutron star according to a generic argument originally made by Blandford (unpublished) and extended in our previous search for such objects in S2 data [6]. The value from Blandford's argument does not depend on the distance to the star or its ellipticity, both of which are highly uncertain.

We find the next milestone by considering the maximum distance to which a signal could be detected and the ellipticity needed to generate a signal of the required strength at that distance. Both quantities are of interest since there are theoretical limits on the ellipticity, and both quantities are functions of the gravitational-wave frequency f and its derivative $\dot{f}$. Figure 41 is a contour plot of both quantities simultaneously, which we explain here in more detail. The Hough transform multi-interferometer upper limits on h_0 are used for illustration because they fall in the middle of the range of values for the different searches (see Fig. 37). The maximum distance $d(f, \dot{f})$ is obtained by equating the 95% confidence upper limits on h_0 for the multiple-interferometer plot in Fig. 31 to the spin-down limit given in Eq. (7). This tacitly assumes that $\dot{f}$ is entirely due to emission of gravitational radiation, which implies the ellipticity given in Eq. (8) regardless of the data and the distance to the source. If we relaxed this assumption, knowing that neutron stars
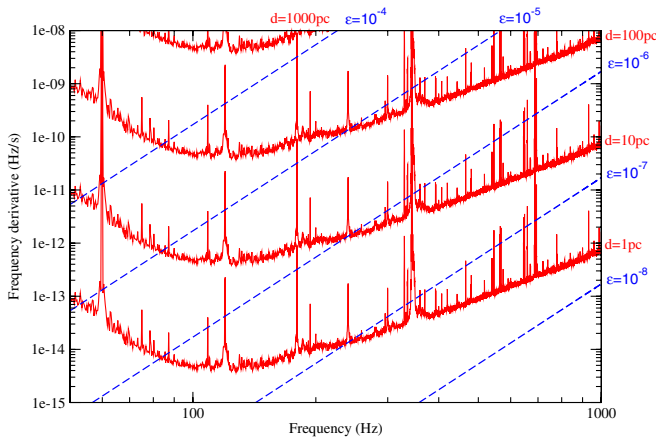

FIG. 41 (color online). Range of the multi-interferometer Hough transform search for neutron stars spinning down solely due to gravitational radiation. This is a superposition of two contour plots. The solid lines (red in the color version) are contours of the maximum distance d at which a neutron star could be detected as a function of gravitational-wave frequency f and its derivative $\dot{f}$. The dashed lines are contours of the corresponding ellipticity $\epsilon(f, \dot{f})$. In concert these quantities tell us the maximum range of the search in terms of various populations (see text for details).

spin down due to electromagnetic wave emission, relativistic particle winds, and other factors as well, the maximum distance and required ellipticity for a given f and $\dot{f}$ would both be reduced. The degree of reduction would, however, be highly uncertain.

We can use the combined contour plot in Fig. 41 to answer questions about the astrophysical significance of our results. Here we ask and answer several salient questions. First, what is the maximum range of the Hough transform search? The answer is obtained from looking at the top of Fig. 41: We could detect isolated pulsars to about 1 kpc, but only for a star radiating at a frequency near 100 Hz and then only if that star has an ellipticity somewhat more than 10^{-4}, which is allowed only in the most extreme equations of state [36–38]. Second, what is the maximum range of detection for a normal neutron star? Normal neutron stars are expected to have $\epsilon < 10^{-6}$ based on theoretical predictions [39]. By tracing the $\epsilon = 10^{-6}$ contour, we find that the maximum range is about 50 pc at the highest frequencies (1 kHz), falling with frequency to less than 2 pc below 100 Hz. Third, what is the maximum range for a recycled millisecond pulsar? Based on the observed sample [22], recycled pulsars usually have small $|\dot{f}|$ values, corresponding to ϵ_{sd} usually less than 10^{-8}. Unfortunately the $\epsilon = 10^{-8}$ contour corresponds to $d < 1$ pc at all frequencies in the LIGO band.

Figure 41 then demonstrates that we have reached a second milestone not achieved in our previous all-sky searches [6,7]: The multi-interferometer Hough transform search could have detected an object at the distance of the nearest known neutron star RX J1856.5-3754, which is about 110–170 pc from Earth [40,41]. We could not have detected that particular star, since the recently observed 7 s rotation period [42] puts the gravitational-wave frequency well out of the LIGO band. But the top of Fig. 41 shows that we could have detected a Crab-like pulsar ($f \approx 100$ Hz, $\dot{f} \approx 10^{-10}$ Hz s^{-1}) at that distance if gravitational radiation dominated its spin-down.

For the ongoing S5 data run, expected to finish data collection in late 2007, several refinements of these methods are under development. The StackSlide and Hough methods can be made more sensitive than PowerFlux by starting with the maximum likelihood statistic (known as the $\mathcal{F}$-statistic [6,10,18]) rather than SFT power. This increases the time-baseline of the coherent step in a hierarchical search, though at increased computational cost. The lower computational cost of the Hough search would be an advantage in this case. Multi-interferometer searches also increase the sensitivity, while reducing outliers (false alarms), without having to increase greatly the size of the parameter space used, as illustrated by the Hough search in this paper. A multi-interferometer version of PowerFlux is under development, as well as hierarchical multi-interferometer searches that use the Hough and StackSlide method on the $\mathcal{F}$-statistic.

Thus, PowerFlux will be the primary tool used for semi-coherent searches using SFTs, while the Hough and StackSlide methods will be used in multi-interferometer hierarchical searches. Strong candidates from the PowerFlux search will be fed into the latter type of search as well. The parameter-space searches described here do not take into account the correlations that exist between points in the four or five dimensional parameter space (including those on the sky). A map of the mismatch between a signal and the parameter-space templates can be used to generate a parameter-space metric to reduce further the number of points needed to conduct a search, a method under development for the hierarchical searches. Finally, the strain noise of the S5 data is lower by about a factor of 2, and the run will accumulate at least 1 yr of science-mode data.

ACKNOWLEDGMENTS

APPENDIX A: POWERFLUX POLARIZATION PROJECTION RELATIONS

The PowerFlux method uses circular and four linear-polarization "projections" to increase sensitivity to different source polarizations [43]. The projections are necessarily imperfect because the interferometer itself is a polarimeter continually changing its orientation with respect to a source on the sky. There is "leakage" of one polarization into another's projection. In this appendix we present the formulae used by PowerFlux to define these imperfect projections and discuss corrections one can make for leakage in follow-up studies of candidates.

As described in Sec. V D 3, the signal estimator used by PowerFlux for frequency bin k and projection polarization angle ψ' is

$$R = \frac{2}{T_{\text{coh}}} \sum_i W_i \frac{P_i}{|F^i_{\psi'(+)}|^2} \Big/ \sum_i W_i, \qquad (A1)$$

where $W_i \equiv |F^i_{\psi'(+)}|^4/(\bar{P}_i)^2$ is the weight for SFT i and $F^i_{\psi'([+/\times])}$ is the antenna pattern factor for a source with $[+, \times]$ polarization with respect to a major axis of polarization angle ψ'.

For a source of true polarization angle ψ and plus/cross amplitudes A_+ and $A_\times$, where $h'_+(t) = A_+ \cos(\omega t + \Phi)$ and $h'_\times(t) = A_\times \sin(\omega t + \Phi)$, the strain amplitudes projected onto the $+$ and $\times$ axes for a polarization angle ψ' are

$$h_+ = A_+ \cos(\omega t)\cos(\Delta\psi) - A_\times \sin(\omega t)\sin(\Delta\psi), \quad (A2)$$

$$h_\times = A_+ \cos(\omega t)\sin(\Delta\psi) + A_\times \sin(\omega t)\cos(\Delta\psi), \quad (A3)$$

where $\Delta\psi \equiv 2(\psi - \psi')$, where the SFT-dependent phase constant Φ_0 has been taken to be zero, for convenience, and where frequency variation of the source during each 30-minute SFT interval has been neglected. Averaging the detectable signal power $(F_{\psi'(+)}h_+ + F_{\psi'(\times)}h_\times)^2$ over one SFT interval i, one obtains approximately (neglecting antenna rotation during the half-hour interval):

$$\begin{aligned}
\langle P_{\text{signal}} \rangle = \tfrac{1}{4}[&(F_+^2 + F_\times^2)(A_+^2 + A_\times^2) \\
&+ (F_+^2 - F_\times^2)(A_+^2 - A_\times^2)\cos(2\Delta\psi) \\
&+ 2F_+ F_\times(A_+^2 - A_\times^2)\sin(2\Delta\psi)].
\end{aligned} \qquad (A4)$$

Note that for a linearly polarized source with polarization angle $\psi = \psi'$ (so that $\Delta\psi = 0$) and amplitude $A_+ = h_0^{\text{Lin}}$, $A_\times = 0$, one obtains

$$\langle P_{\text{signal}} \rangle = \tfrac{1}{2}F_+^2 (h_0^{\text{Lin}})^2, \qquad (A5)$$

and that for a circularly polarized source of amplitude $A_+ = A_\times = h_0^{\text{Circ}}$,

$$\langle P_{\text{signal}} \rangle = \tfrac{1}{2}(F_+^2 + F_\times^2)(h_0^{\text{Circ}})^2, \qquad (A6)$$

as expected.

For an average of powers from many SFT's, weighted according to detector noise and antenna pattern via W_i, the expectation value of the signal estimator depends on

$$\langle P_{\text{det}} \rangle = \langle P_{\text{signal}} \rangle + \langle n(\psi')^2 \rangle + 2\langle P_{\text{signal}} n(\psi') \rangle, \qquad (A7)$$

where n_i is the expected power from noise alone, where $\langle P_{\text{signal}} n \rangle$ is assumed to vanish (signal uncorrelated with noise), and where the frequency bin index k is omitted for simplicity.

For a true source with parameters ψ, A_+, and $A_\times$, this expectation value can be written:

$$\begin{aligned}
\langle P_{\text{det}} \rangle = \langle n(\psi')^2 \rangle + \tfrac{1}{4}[&(1 + \beta_2)(A_+^2 + A_\times^2) \\
&+ (1 - \beta_2)(A_+^2 - A_\times^2)\cos(2\Delta\psi) \\
&+ 2\beta_1(A_+^2 - A_\times^2)\sin(2\Delta\psi)],
\end{aligned} \qquad (A8)$$

where the correction coefficients

$$\beta_1 = \frac{\sum_i W_i F_\times / F_+}{\sum_i W_i}, \tag{A9}$$

$$\beta_2 = \frac{\sum_i W_i F_\times^2 / F_+^2}{\sum_i W_i}, \tag{A10}$$

depend implicitly on ψ' through F_+ and $F_\times$.

For a linearly polarized source with polarization angle $\psi = \psi'$, one obtains

$$\langle P_{\text{det}} \rangle = \langle n(\psi')^2 \rangle + \tfrac{1}{2}(h_0^{\text{Lin}})^2, \tag{A11}$$

and for a circularly polarized source one obtains

$$\langle P_{\text{det}} \rangle = \langle n(\psi')^2 \rangle + \tfrac{1}{2}(h_0^{\text{Circ}})^2(1 + \beta_2). \tag{A12}$$

These formulae permit corrections for polarization leakage to be applied for a hypothetical source, allowing for estimation of ψ, A_+, and $A_\times$ from a sampling of polarization projection measurements. In practice, however, the calculation of the β coefficients is computationally costly in an all-sky search and is disabled by default. Instead, upper limits on linearly polarized sources (worst-case pulsar inclination) are derived from the maximum limit over all four linear-polarization projections, as described in Sec. V D 3. In follow-up investigations of outliers, however, these formulae permit greater discrimination of candidates, now in use for PowerFlux searches of the data from the ongoing S5 data run.

APPENDIX B: STACKSLIDE POWER AND STATISTICS

1. Approximate form for the StackSlide Power

It is useful to have an analytic approximation for the StackSlide Power P. For a single SFT (dropping the SFT index i) expressing the phase in a first-order Taylor expansion about the midpoint time, $t_{1/2}$, of the interval used to generate a SFT, we can write

$$\phi(t) \cong \phi_{1/2} + 2\pi f_{1/2}(t - t_{1/2}), \tag{B1}$$

where $\phi_{1/2}$ and $f_{1/2}$ are the phase and frequency at time $t_{1/2}$. Treating the values of F_+ and $F_\times$ as constants equal to their values at time $t_{1/2}$, the signal strain at discrete time t_j is approximately

$$\begin{aligned} h_j &\cong F_+ A_+ \cos(\phi_0 + 2\pi f_{1/2} t_j) \\ &\quad + F_\times A_\times \sin(\phi_0 + 2\pi f_{1/2} t_j), \end{aligned} \tag{B2}$$

where $j = 0$ gives the start time of the SFT, and ϕ_0 is the approximate phase at the start of the SFT (not the initial phase at the start of the observation), i.e.,

$$\phi_0 \equiv \phi_{1/2} - 2\pi f_{1/2}(T_{\text{coh}}/2). \tag{B3}$$

Using these approximations, the discrete Fourier transform, given by Eq. (12), of h_j is

$$\begin{aligned} \frac{\tilde{h}_k}{T_{\text{coh}}} &\cong e^{i\phi_0}\left[\frac{F_+ A_+}{2} - i\frac{F_\times A_\times}{2}\right] \\ &\quad \times \left[\frac{\sin(2\pi\Delta\kappa)}{2\pi\Delta\kappa} + i\frac{1 - \cos(2\pi\Delta\kappa)}{2\pi\Delta\kappa}\right], \end{aligned} \tag{B4}$$

where $\Delta\kappa \equiv \kappa - k$ and $\kappa \equiv f_{1/2} T_{\text{coh}}$ is usually not an integer. Equation (B4) holds for $0 < \kappa < M/2$ and $|\kappa - k| \ll M$, which is true for all of the frequencies over which we search.

If the discrete time samples of the data from the detector consist of a signal plus noise the expected value of P is approximated by

$$P \cong P_0 + \tfrac{1}{2}\langle d^2 \rangle, \tag{B5}$$

where the mean value of P_0 is 1 and its standard deviation is $1/\sqrt{N}$ due to the normalization used, and

$$\langle d^2 \rangle \cong \left[A_+^2\left\langle \frac{F_+^2}{S_k}\frac{\sin^2(\pi\Delta\kappa)}{\pi^2\Delta\kappa^2}\right\rangle + A_\times^2\left\langle \frac{F_\times^2}{S_k}\frac{\sin^2(\pi\Delta\kappa)}{\pi^2\Delta\kappa^2}\right\rangle\right]T_{\text{coh}}, \tag{B6}$$

is an approximate form for the square of the optimal SNR defined in Eq. (71) in Ref. [18] averaged over SFTs (i.e., the angle brackets on $\langle d^2 \rangle$ represent an average over SFTs) and where for each SFT the index k is the nearest integer value to κ. Thus, the relevant range for $\Delta\kappa$ is 0 to 0.5, corresponding to a frequency mismatch of 0 to 1/2 of an SFT frequency bin.

2. StackSlide statistics

It can be seen from Eq. (16) that, for Gaussian noise in the absence of a signal, $2NP$ is a χ^2 variable with $2N$ degrees of freedom [15]. Thus, the quantity

$$\varrho \equiv 2NP \tag{B7}$$

follows the χ^2 distribution:

$$\mathcal{P}(\varrho; N)d\varrho = \frac{1}{2^N\Gamma(N)}\varrho^{N-1}e^{-\varrho/2}d\varrho. \tag{B8}$$

When a signal is present, ϱ follows a noncentral χ^2 distribution with $2N$ degrees of freedom and a noncentrality parameter $N\langle d^2 \rangle$ such that

$$\mathcal{P}(\varrho; N\langle d^2 \rangle)d\varrho = \frac{I_{N-1}(\sqrt{\varrho N\langle d^2 \rangle})}{(N\langle d^2 \rangle)^{N-1}}\varrho^{N-1/2}e^{-(\varrho + N\langle d^2 \rangle)/2}d\varrho, \tag{B9}$$

where the form given here is based on that given in [44], and I_{N-1} is the modified Bessel function of the first kind and order $N - 1$.

The distribution described by Eqs. (B8) and (B9) can be used to find the minimum optimal signal-to-noise ratio that can be detected using the StackSlide search for fixed false-alarm and false-dismissal rates, for a targeted search. For a 1% false-alarm rate, a 10% false-dismissal rate, and large

N Eqs. (B7) and (B9) give $\langle d^2 \rangle = 7.385/\sqrt{N}$ (see also [15]), while averaging Eq. (B6) independently over the source sky position, inclination angle, polarization angle, and mismatch in frequency gives $\langle d^2 \rangle = 0.7737(4/25) \times (h_0^2 T_{\mathrm{coh}}/S)$ (see also Eq. 5.35 in [10]). Equating these and solving for h_0, the characteristic amplitude for a targeted StackSlide search with a 1% false-alarm rate, 10% false-dismissal rate is

$$\langle h_0 \rangle_{\mathrm{targeted}} = 7.7\sqrt{S}/(T_{\mathrm{coh}} T_{\mathrm{obs}}^*)^{1/4}, \qquad \text{(B10)}$$

where $T_{\mathrm{obs}}^* = N T_{\mathrm{coh}}$ is the actual duration of the data, which is shorter than the total observation time, T_{obs}, because gaps exist in the data for times when the detectors were not operating in science mode. Comparing this expression with Eq. 5.35 in [10] the StackSlide characteristic amplitude given in Eq. (B10) is found to be about 10%

lower than a similar estimate for the standard Hough search. Note that in this paper an improved version of the Hough method is presented. Also, in this paper an all-sky search for the loudest StackSlide Power is carried out, covering up to 1.88×10^9 templates, and only the loudest StackSlide Power is returned from the search, corresponding to a false-alarm rate of 5.32×10^{-10}. Furthermore, the upper limits are found by injecting a family of signals, each of which has a StackSlide Power drawn from a different noncentral chi-squared distribution. Using the results from Sec. VII, for an all-sky StackSlide search the 95% confidence all-sky upper limits are found empirically to be approximately given by

$$\langle h_0 \rangle_{\mathrm{all\text{-}sky}} = 23\sqrt{S}/(T_{\mathrm{coh}} T_{\mathrm{obs}}^*)^{1/4}. \qquad \text{(B11)}$$

[1] A. Abramovici *et al.*, Science **256**, 325 (1992).

[2] B. Barish and R. Weiss, Phys. Today **52**, 44 (1999).

[3] B. Abbott *et al.* (LIGO Scientific Collaboration), Phys. Rev. D **69**, 102001 (2004).

[4] B. Abbott *et al.* (LIGO Scientific Collaboration), M. Kramer, and A. G. Lyne, Phys. Rev. Lett. **94**, 181103 (2005).

[5] B. Abbott *et al.* (LIGO Scientific Collaboration), M. Kramer, and A. G. Lyne, Phys. Rev. D **76**, 042001 (2007).

[6] B. Abbott *et al.* (LIGO Scientific Collaboration), arXiv:gr-qc/0605028 [Phys. Rev. D (to be published)].

[7] B. Abbott *et al.* (LIGO Scientific Collaboration), Phys. Rev. D **72**, 102004 (2005).

[8] The Einstein@Home project is built upon the BOINC (Berkeley Open Infrastructure for Network Computing) architecture described at http://boinc.berkeley.edu/.

[9] Results from the distributed computing project Einstein@Home can be found at http://einstein.phys.uwm.edu/.

[10] B. Krishnan, A. M. Sintes, M. A. Papa, B. F. Schutz, S. Frasca, and C. Palomba, Phys. Rev. D **70**, 082001 (2004).

[11] M. A. Papa, B. F. Schutz, and A. M. Sintes, in *Gravitational Waves: A Challenge to Theoretical Astrophysics*, ICTP Lecture Notes Series Vol. III, edited by V. Ferrari, J. C. Miller, and L. Rezzolla (ICTP, Trieste, Italy, 2001), p. 431.

[12] P. Brady and T. Creighton, Phys. Rev. D **61**, 082001 (2000).

[13] C. Cutler, I. Gholami, and B. Krishnan, Phys. Rev. D **72**, 042004 (2005).

[14] P. Brady, T. Creighton, C. Cutler, and B. F. Schutz, Phys. Rev. D **57**, 2101 (1998).

[15] G. Mendell and M. Landry, LIGO technical document LIGO-T050003, 2005, available in http://admdbsrv.ligo.caltech.edu/dcc/.

[16] C. Palomba, P. Astone, and S. Frasca, Classical Quantum Gravity **22**, S1255 (2005).

[17] V. Dergachev, LIGO technical document LIGO-T050186, 2005, available in http://admdbsrv.ligo.caltech.edu/dcc/.

[18] P. Jaranowski, A. Królak, and B. F. Schutz, Phys. Rev. D **58**, 063001 (1998).

[19] D. Sigg (LIGO Scientific Collaboration), Classical Quantum Gravity **23**, S51 (2006).

[20] LSC Algorithms and LALapps Applications software libraries available at http://www.lsc-group.phys.uwm.edu/daswg/.

[21] C. Palomba, Mon. Not. R. Astron. Soc. **359**, 1150 (2005).

[22] R. N. Manchester, G. B. Hobbs, A. Teoh, and M. Hobbs, Astron. J. **129**, 1993 (2005); see also http://www.atnf.csiro.au/research/pulsar/psrcat/.

[23] S. D. Mohanty, Classical Quantum Gravity **19**, 1513 (2002).

[24] S. D. Mohanty and S. Mukherjee Classical Quantum Gravity **19**, 1471 (2002).

[25] B. Krishnan, LIGO technical document T040144, 2004, available in http://admdbsrv.ligo.caltech.edu/dcc/.

[26] X. Siemens *et al.*, Classical Quantum Gravity **21**, S1723 (2004).

[27] A. Dietz *et al.*, LIGO technical document LIGO-T050262, 2005, available in http://admdbsrv.ligo.caltech.edu/dcc/.

[28] The condor package is available at http://www.cs.wisc.edu/condor/.

[29] The Matlab program is available at http://www.mathworks.com.

[30] P. V. C. Hough, in International Conference on High Energy Accelerators and Instrumentation, CERN, 1959 (unpublished).

[31] P. V. C. Hough, U.S. Patent No. 3 069 654, 1962.

[32] J. Illingworth and J. Kittler, Computer Vision, Graphics, and Image Processing **44**, 87 (1988).

[33] B. Krishnan and A. M. Sintes, LIGO technical document T070124, 2007, available in http://admdbsrv.ligo.caltech.edu/dcc/.

[34] G. J. Feldman and R. D. Cousins, Phys. Rev. D **57**, 3873 (1998).

[35] See EPAPS Document No. E-PRVDAQ-76-127722 for numerical values of upper limits derived for each method in 0.25 Hz bands in the range 50–1000 Hz. For more information on EPAPS, see http://www.aip.org/pubservs/epaps.html.

[36] B. J. Owen, Phys. Rev. Lett. **95**, 211101 (2005).

[37] R. X. Xu, Astrophys. J. **596**, L59 (2003).

[38] M. Mannarelli, K. Rajagopal, and R. Sharma, arXiv:hep-ph/0702021 [Phys. Rev. D (to be published)].

[39] G. Ushomirsky, C. Cutler, and L. Bildsten, Mon. Not. R. Astron. Soc. **319**, 902 (2000).

[40] F. M. Walter and J. Lattimer, Astrophys. J. **576**, L145 (2002).

[41] M. H. van Kerkwijk and D. L. Kaplan, Astrophys. Space Sci. **308**, 191 (2007).

[42] A. Tiengo and S. Mereghetti, Astrophys. J. **657**, L101 (2007).

[43] V. Dergachev and K. Riles, LIGO technical document, LIGO-T050187, 2005, available in http://admdbsrv.ligo.caltech.edu/dcc/.

[44] P. Jaranowski and A. Królak, Phys. Rev. D **61**, 062001 (2000).